# Structural basis for assembly and function of the Nup82 complex in the nuclear pore scaffold

Monika Gaik,[1]* Dirk Flemming,[1]* Alexander von Appen,[2]* Panagiotis Kastritis,[2] Norbert Mücke,[3] Jessica Fischer,[1] Philipp Stelter,[1] Alessandro Ori,[2] Khanh Huy Bui,[2] Jochen Baßler,[1] Elisar Barbar,[4] Martin Beck,[2] and Ed Hurt[1]

[1]Biochemistry Center of Heidelberg University, D-69120 Heidelberg, Germany
[2]Structural and Computational Biology Unit, European Molecular Biology Laboratory, D-69117 Heidelberg, Germany
[3]Division of Biophysics of Macromolecules, German Center Research Center, D-69120 Heidelberg, Germany
[4]Department of Biochemistry and Biophysics, Oregon State University, Corvallis, OR 97331

Nuclear pore complexes (NPCs) are huge assemblies formed from ∼30 different nucleoporins, typically organized in subcomplexes. One module, the conserved Nup82 complex at the cytoplasmic face of NPCs, is crucial to terminate mRNA export. To gain insight into the structure, assembly, and function of the cytoplasmic pore filaments, we reconstituted in yeast the Nup82–Nup159–Nsp1–Dyn2 complex, which was suitable for biochemical, biophysical, and electron microscopy analyses. Our integrative approach revealed that the yeast Nup82 complex forms an unusual asymmetric structure with a dimeric array of subunits. Based on all these data, we developed a three-dimensional structural model of the Nup82 complex that depicts how this module might be anchored to the NPC scaffold and concomitantly can interact with the soluble nucleocytoplasmic transport machinery.

## Introduction

Nuclear pore complexes (NPCs), which are integrated into the double nuclear membrane, serve as the exclusive gateways to guide molecules between the nucleus and the cytoplasm. To perform its role in nucleocytoplasmic transport, the NPC has adopted a supramolecular structure, ∼60 MD in yeast and 120 MD in human, which is composed of multiple copies of ∼30 different structurally conserved nucleoporins (Doye and Hurt, 1997; Rout et al., 2000). The vast majority of nucleoporins is symmetrically arranged within the NPC, but a few of them are located asymmetrically at either the cytoplasmic or nucleoplasmic face of the NPC (Rout et al., 2000). EM revealed that a single NPC exhibits a characteristic structural appearance with an overall eightfold rotational symmetry along the transport axis. Directly embedded in the nuclear membrane is the central spoke–ring scaffold (inner pore ring), which anchors the nuclear and cytoplasmic ring, from which peripheral elements, the nuclear basket, and cytoplasmic filaments emanate (Fahrenkrog and Aebi, 2003; Beck et al., 2004). Within the center of the NPC is a channel-like structure, which is filled by a meshwork of unstructured phenylalanine-glycine (FG)–rich repeat sequences that are present in several nucleoporins and are thought to form the permeability barrier of the NPC (Frey et al., 2006; Lim et al., 2007). A hallmark of the FG repeat domains is that they can bind with low affinity to shuttling nuclear transport receptors, which allows them to translocate their bound cargoes between the nucleus and cytoplasm.

Most of the nucleoporins are part of discrete NPC subcomplexes, which form the building blocks of the nuclear pore (Rout et al., 2000). A well-characterized NPC module is the Nup82 complex, which is exclusively located at the cytoplasmic side of the NPC and predominantly involved in nuclear mRNA export (Grandi et al., 1995a; Kraemer et al., 1995; Belgareh et al., 1998; Noble et al., 2011). Initially, the purified Nup82 complex was suggested to consist of three subunits, Nup82, Nsp1, and Nup159, which bind to each other through their C-terminal domains (CTDs) and involve coiled-coil interactions

*M. Gaik, D. Flemming, and A. von Appen contributed equally to this paper.

Correspondence to Ed Hurt: ed.hurt@bzh.uni-heidelberg.de; or Martin Beck: martin.beck@embl.de

Abbreviations used in this paper: 5-FOA, 5-fluoro-orotic acid; ACN, acetonitrile; AQUA, absolutely quantified; CD, circular dichroism; CTD, C-terminal domain; DID, dynein interaction domain; DSG, disuccinimidyl-glutarate; DSS, disuccinimidyl-suberate; FA, formic acid; MALS, multiangle light scattering; MS, mass spectrometry; NPC, nuclear pore complex; SA, simulated annealing; SEC, size-exclusion chromatography; SRM-MS, selected reaction monitoring MS; TEV, tobacco etch virus; UPLC, ultraperformance liquid chromatography; XL-MS, cross-linking MS.



The Rockefeller University Press $30.00
J. Cell Biol. Vol. 208 No. 3 283–297
www.jcb.org/cgi/doi/10.1083/jcb.201411003

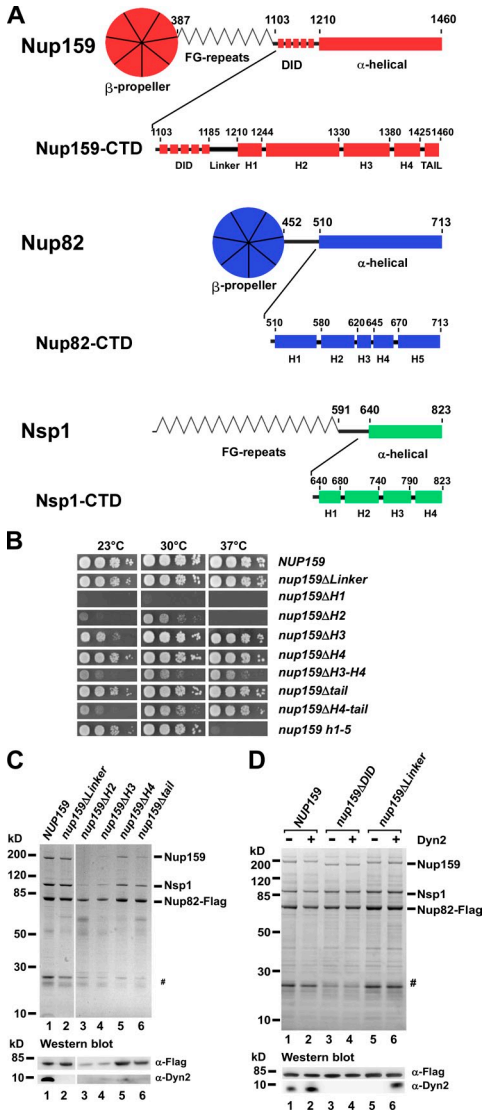


Figure 1. **The Nup159 CTD is important for Nup82 complex assembly and incorporation into the NPC scaffold.** (A) Domain architecture of yeast Nup159, Nup82, and Nsp1. Amino acid positions are indicated above, and sequence motifs are given below the drawings. α-Helically predicted C-terminal domains (CTD) are shown in enlarged schemes (not in scale) according to secondary structure predictions. (B) Growth analysis of wild-type and *nup159* deletion strains. A *nup159Δ* shuffle strain was transformed with the indicated *nup159* mutant constructs under the control of the endogenous *NUP159* promoter. It was spotted in 10-fold serial dilutions onto synthetic dextrose complete medium + 5-FOA plates and incubated at the indicated temperatures for 5 d. (C and D) Mutations in the Nup159 CTD impair in vivo Nup82 complex assembly and Dyn2 recruitment. Tandem affinity-purified Nup82-Flag-TEV-ProtA eluates derived from cells expressing wild-type or the indicated Nup159-CTD mutant constructs were analyzed by SDS-PAGE and Coomassie staining (top) or Western blotting using anti-Flag (to detect Nup82) and anti-Dyn2 antibodies (bottom). Indicated on the right are the Nup159, Nsp1, and Nup82-Flag bands; #, TEV protease. White lines indicate that intervening lanes have been spliced out. (D) The *nup159ΔLinker* mutant can only bind to Dyn2, when overexpressed. See also Fig. S1, Fig. S2 A, and Tables S1 and S2.

(Gorsch et al., 1995; Grandi et al., 1995a; Del Priore et al., 1997; Belgareh et al., 1998). Later on, additional interacting factors of the Nup82 complex such as Nup116 and Gle2 (Bailer et al., 2000), Dbp5 and Gle1 (Hodge et al., 1999; Weirich et al., 2004; Noble et al., 2011), and Dyn2 (Stelter et al., 2007) were discovered. The Nup82 complex appears to have additional roles not related to nucleocytoplasmic transport, e.g., in the inheritance of NPCs (Makio et al., 2013).

The most prominent member of the Nup82 complex is Nup159, which carries a conserved β-propeller domain at its N terminus that recruits the DEAD-box RNA helicase Dbp5 (Fig. 1 A; Hodge et al., 1999; Schmitt et al., 1999). This interaction is structurally well understood and crucial for terminating messenger RNP export at the cytoplasmic pore filaments, most likely by dismantling the messenger RNPs (Weirich et al., 2004; Tran et al., 2007). Nup159's α-helically predicted CTD is essential for NPC targeting, Nup82 complex assembly, and NPC biogenesis (Del Priore et al., 1997; Belgareh et al., 1998). Similar to Nup159, Nup82 carries a β propeller at the N terminus, which is involved in binding to other nucleoporins (Fig. 1 A). The crystallized Nup82's β propeller together with a fragment of Nup116 (autocatalytic domain) and a short tail fragment of Nup159 were recently reported, clarifying how these nucleoporins interact with each other (Yoshida et al., 2011). Besides the β-propeller, Nup82 possesses a predicted α-helical segment in the C-terminal half, and both domains are crucial for Nup82 function (Grandi et al., 1995a; Hurwitz and Blobel, 1995). Nsp1 is the third member of the complex, but it is also present in another subcomplex (Nsp1–Nup49–Nup57–Nic96), which is thought to be involved in forming the central transport channel (Hurt, 1988; Grandi et al., 1995b). Nsp1 has an unstructured region consisting of numerous FG repeats in the N terminus and four predicted coiled-coil regions (coil 1–4) in its essential CTD (Fig. 1 A). In vitro reconstitution revealed that coiled-coil region 2 of Nsp1 binds to Nup57 and Nup82 in a competitive manner (Bailer et al., 2001).

In yeast, the small protein dynein light chain (Dyn2) is a further subunit of the Nup82 complex (Stelter et al., 2007). Dyn2 binds to a series of five consecutive short linear QT motifs (also called $DID_{Nup159}$) inserted between the FG repeats and CTD of Nup159. Dyn2 was proposed to act as molecular glue stabilizing the Nup82 complex at the NPC (Stelter et al., 2007; Barbar, 2008). Dyn2 is the yeast orthologue of the molecular hub protein DLC8, present in the dynein motor complex (Barbar, 2008), which forms a stable homodimer with two binding grooves for recognition motifs, found in some disordered proteins (e.g., Bim, neuronal nitric oxide synthase, and Swallow). Upon DLC8 binding to intermediate chains of the dynein motor complex, adjacent coiled-coil regions undergo rearrangements, leading to self-dimerization and complex stabilization (Nyarko and Barbar, 2011). EM showed that upon binding of five Dyn2 dimers to $DID_{Nup159}$, an ∼20-nm-long rigid rodlike structure of two dimerized $DID_{Nup159}$ motifs is formed (Stelter et al., 2007). Time-dependent assembly of the Nup82 complex was followed in vivo, revealing that Dyn2 was incorporated into the Nup82 complex with a delay (Stelter et al., 2012).

In higher eukaryotes, nucleoporins Nup88 (Nup82), Nup214 (Nup159), and Nup62 (Nsp1), located at the cytoplasmic side of the NPC, are thought to constitute the orthologous vertebrate complex (Kraemer et al., 1994; Fornerod et al., 1997; Bui et al., 2013). Nup88 and Nup214 have a similar domain organization when compared with the yeast Nup82 and Nup159, respectively, with N-terminal β propeller followed by α-helical

domains. Nup214 and Nup159 comprise additional FG repeats (Napetschnig et al., 2007). Interestingly, both *NUP214* and *NUP88* in human are often linked to cancer (Köhler and Hurt, 2010), such that Nup88 is overexpressed in a broad spectrum of human malignant tumors (Martínez et al., 1999), and *NUP214* is frequently found in a chromosomal rearrangements related to leukemia (von Lindern et al., 1992). Additionally, Nup358/RanBP2, which only exists in higher eukaryotes and is absent from fungi, interacts with Nup88 and forms a 36-nm-thick filament at the cytoplasmic pore fibers (Delphin et al., 1997; Bernad et al., 2004). There are reports that the network of interactive Nup88–Nup62–Nup214–Nup358 is involved in nuclear mRNA export that recruits a DEAD-box helicase (Ddx19; Napetschnig et al., 2007; Montpetit et al., 2011). Moreover, a role of Nup214 in the import of proteins carrying a classical NLS has been suggested (van Deursen et al., 1996).

To study the structure and assembly of the cytoplasmic pore filaments, we used a method to assemble in vivo and subsequently isolate the essential structural core of the Nup82 module. Biochemistry and subsequent multiangle light scattering (MALS), analytical ultracentrifugation, and quantitative mass spectrometry (MS; selected reaction monitoring MS [SRM-MS]) measurements suggested that the yeast Nup82 complex forms an unusual asymmetric structure with a dynamic dimeric array of subunits. Electron tomography revealed that the Nup82 complex consists of a 20-nm Dyn2-DID$_{Nup159}$ stalk, from which an asymmetric head structure emerges that integrates both the β propeller and α-helical domain of Nup82 molecules as well as the α-helical C domains of Nup159 and Nsp1. Based on the yeast 3D model, we specify the orthologous Nup88–Nup214 complex in the electron tomography map of the human NPC. The unusual structure of the Nup82 complex may explain how it is anchored to the NPC and at the same time can protrude its FG repeats toward the central transport channel.

## Results

### Essential α-helical segment H1 in Nup159-CTD required for self-dimerization and Nup82 complex assembly

To gain insight in the mechanism of Nup82 complex assembly, we focused on the essential Nup159 subunit, which is predicted to consist of four consecutive domains, (1) an N-terminal β propeller that binds the RNA helicase Dbp5, (2) an array of FG-rich repeat sequences that interact with transport receptors, (3) the dynein interaction domain (DID) motif, a tandem arrangement of five consecutive Dyn2 binding motifs, and (4) an α-helically predicted C domain that includes coiled-coil motifs (Fig. 1 A).

To study which part of the Nup159 CTD is required for Nup82 complex assembly, we performed a biocomputational directed mutational analysis. Based on multiple sequence alignment, secondary structure prediction, and coiled-coil predictions, the Nup159 CTD is well conserved among fungi (Fig. 2 A and Fig. S1), but also homologous to an α-helically predicted sequence in the respective region of vertebrate Nup214 (not depicted). According to this classification, we define conserved subregions in the Nup159 CTD, (a) linker sequence after the DID motif, (b) α-helical predicted regions 1–4 (H1–H4), and (c) tail peptide (tail; Fig. 1 A). Within the α-helical segments H1–H4, a repeated pattern, hxxhcxc, of hydrophobic (h) and charged (c) amino acid residues, referred to as heptad repeats, can be observed, suggestive of coiled-coil interactions. Similarly,

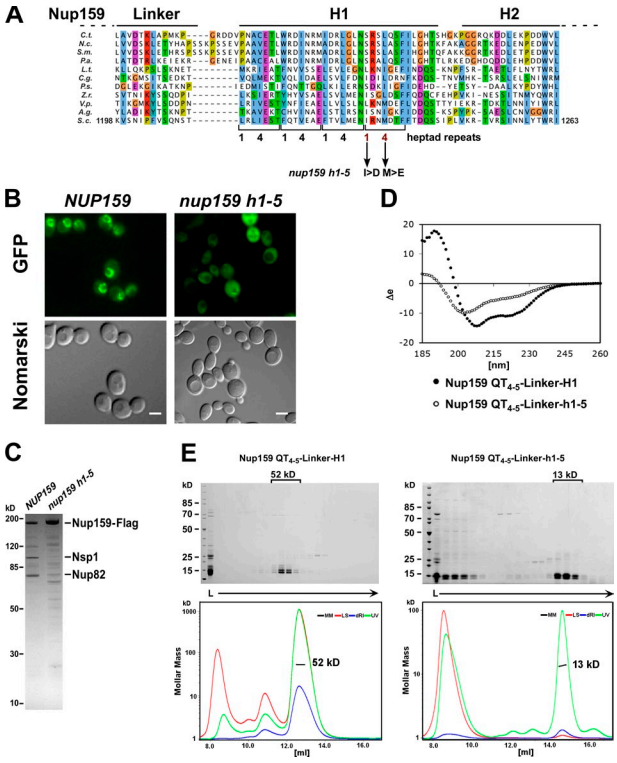


Figure 2. **Heptad repeats in the H1 subdomain of Nup159-CTD are crucial for self-dimerization and Nup82 complex assembly.** (A) Multisequence alignment of Nup159 CTDs from the indicated species: *C.t*, *Chaetomium thermophilum*; *N.c.*, *Neurospora crassa*; *S.m.*, *Sordaria macrospora*; *P.a.*, *Podospora anserina*; *L.t.*, *Lachancea thermotolerans*; *C.g.*, *Candida glabrata*; *P.s.*, *Pichia stipitis*; *Z.r.*, *Zygosaccharomyces rouxii*; *V.p.*, *Vanderwaltozyma polyspora*; *A.g.*, *Ashbya gossypii*; *S.c.*, *Saccharomyces cerevisiae*. The Nup159 H1 subdomain has conserved heptad repeats with hydrophobic residues at position 1 and 4 (indicated below). Arrows point to the amino acid mutations in the *nup159 h1-5* mutant (*Ile1232>Asp/Met1235>Glu*). The default color scheme of ClustalX/Jalview was used with e.g., hydrophobic residues in blue, acidic residues in violet, and basic residues in red. (B) Subcellular location of wild-type Nup159 and mutant Nup159 h1-5, both labeled with GFP, in yeast cells grown at 30°C. Mutant *nup159 h1-5* has lost the characteristic nuclear rim (NPC) staining. Bars, 2 µm. (C) *nup159 h1-5* is defective in Nup82 complex assembly. Affinity-purified Nup159-Flag-TEV-ProtA eluates derived from cells grown at 30°C and expressing either wild-type or mutant *nup159 h1-5* were analyzed by SDS-PAGE and Coomassie staining. Nup159 h1-5-Flag-TEV-ProtA was not coenriched for Nup82 and Nsp1. (D) Far UV CD spectra of *E. coli* expressed and affinity-purified Nup159-QT$_{4–5}$-Linker-H1 and Nup159-QT$_{4–5}$-Linker-*h1-5* mutant constructs. Nup159-H1 exhibits an overall α-helical structure indicated by two minima at 208 and 222 nm. In contrast, the Nup159-*h1-5* mutant construct is fully disordered as shown by a single signal at 203 nm and absence of a signal at 222 nm. (E) Recombinant Nup159-H1 subdomain forms a homo-oligomer, which is disassembled upon mutating the heptad repeat pattern. The indicated Nup159-QT$_{4–5}$-Linker-H1 wild-type and mutant fragments (see also D) were affinity purified and separated by SEC followed by SDS-PAGE and Coomassie staining (top) or analyzed by MALS (bottom). Intact Nup159-QT$_{4–5}$-Linker-H1 construct eluted as a homotetramer (52 kD), whereas Nup159-QT$_{4–5}$-Linker-*h1-5* mutant construct was monomeric (13 kD) but also found in large aggregates. The data shown are from a single representative experiment out of two repeats. See also Fig. S1. dRI, differential refractive index; L, load; LS, light scattering; MM, molecular mass.

Nup82 and Nsp1 exhibit a predicted α-helical organization in their C-terminal domains (Fig. 1 A).

According to these subregions, we made nested deletions and tested them in a *nup159Δ* shuffle strain for complementation of the otherwise nonviable *nup159*-null mutant (see Materials and methods). Notably, most of these Nup159-CTD mutants were viable (e.g., *nup159ΔH4)* at 30°C, except *nup159ΔH1* (*Δ1,210–1,244*), which exhibited lethality at all tested temperatures (Fig. 1 B). In contrast, several of the *nup159* deletion strains showed a temperature-sensitive growth defect (Fig. 1 B). In contrast, several of the *nup159* deletion strains showed a temperature-sensitive growth defect (Fig. 1 B). When tested by Western blotting, some of these mutants were rather normally expressed, whereas other *nup159* mutant alleles, in particular those showing a very slow growth phenotype (*nup159ΔH2)*, exhibited reduced Nup159 levels (Fig. S2 A). However, by combining distinct *nup159* deletions intramolecularly, the observed phenotypic growth defects were enhanced (e.g., *nup159ΔH3-ΔH4* grew slower at all tested temperatures; *nup159ΔH4-Δtail* was cold sensitive, as a result of distorted structure of the Nup82 complex, see following paragraph; Fig. 1 B). We conclude that the essential Nup159 CTD harbors discrete subregions, which apparently tolerate severe mutations, except the H1 domain, which is essential for Nup159 function (see following paragraph).

Next, we investigated how Nup82 complex assembly is altered in vivo by affinity purification of Nup82-Flag–tobacco etch virus (TEV)–ProtA from cells expressing the different Nup159-CTD mutant proteins. Some of the viable mutants such as *nup159ΔH2* or *nup159ΔH3* are impaired in Nup82 complex assembly, whereas others, e.g., *nup159Δlinker* and *nup159ΔH4*, still allowed isolation of an apparently regular Nup82–Nup159–Nsp1 complex. However, in the case of *nup159Δlinker*, Dyn2 recruitment was disturbed, which could be reversed by Dyn2 overexpression (Fig. 1, C and D). This unexpected finding suggests that the linker sequence upstream of H1 is critical for efficient Dyn2 recruitment at the $DID_{Nup159}$, which could mean that DID and H1 require a certain distance for optimal Dyn2 binding.

To elucidate the essential function of Nup159-H1, we sought to disturb its heptad repeat pattern by site-specific mutagenesis of conserved hydrophobic residues to charged amino acids at position 1 or 4. Notably, the *nup159 I1232>D/M1235>*E double mutation within H1 (called *h1-5*) generated a strong temperature-sensitive phenotype (Fig. 1 B), which in consequence impaired Nup82 complex assembly and caused a mislocalization of Nup159 to the cytoplasm (Fig. 2, B and C). Moreover, another heptad repeat mutant in H1, *nup159 L1228>D/M1235>E*, caused a lethal phenotype at all temperatures tested (unpublished data).

To gain information on the physicochemical properties of Nup159-H1 and its possibility to self-dimerize through a coiled-coil interaction, we expressed a construct containing the last two Dyn2 binding (QT) motifs of $DID_{Nup159}$ followed by the linker sequence and H1 in *Escherichia coli* (Fig. 2 A and Fig. 1 A). The purification of this minimal construct yielded a soluble protein, which was subjected to circular dichroism (CD) in the absence of Dyn2. This measurement showed that the construct forms an α-helical structure with a stability similar to a canonical coiled coil such as a GCN4 leucine zipper construct (melting temperature > 50°C; unpublished data; Thompson et al., 1993). Consistent with this finding, MALS measurements indicate that the α-helical Nup159-H1 ($QT_{4–5}$-Linker-H1) can self-interact to form an apparent homotetramer. However, the construct with the double point mutation (*h1-5*) was fully disordered and monomeric, or aggregated (Fig. 2, D and E). Thus, Nup159-H1 appears to form a four-stranded coiled coil when expressed in *E. coli*, similar to what has been found for the engineered GCN4 leucine zipper constructs (Harbury et al., 1993). We conclude that in vivo Nup159 can self-dimerize via H1 and by a flexible linker region assures the subsequent binding of Dyn2 to the five QT motifs on $DID_{Nup159}$ that eventually stabilizes the entire Nup159 homodimer. Thus, self-dimerization of Nup159-H1 and its proper position in respect to $DID_{Nup159}$ may be key for Nup82 complex formation and assembly into the NPC in yeast.

## Reconstitution of simplified Nup82 complexes

Although the endogenous tandem affinity purification–purified Nup82 complex from yeast was well behaved during biochemical investigations (Stelter et al., 2007), we were not able to estimate its precise molecular weight and accordingly its subunit stoichiometry (not depicted), as a result of the presence of the natively unfolded and flexible FG repeat sequences on Nup159 and Nsp1 (Fig. 1 A). We therefore considered purification of a Nup82 complex devoid of FG repeat sequences. For this purpose, the genes encoding full-length Nup82 (tagged with Flag-TEV-ProtA), Nup159 lacking the FG repeats (Nup159ΔFG) or lacking both N-terminal β propeller and FG repeats (Nup159C), Nsp1 devoid of FG repeats (Nsp1C), and Dyn2 were placed under the control of the inducible *GAL1* promoter, and all four ORFs were coexpressed in yeast by shifting cells from glucose- to galactose-containing medium (see Materials and methods).

To find out which of these constructs are functional and incorporated into the NPC, we performed complementation and intracellular location experiments. We focused on the *nup159* deletion constructs because Nsp1's FG repeat domain can be deleted without impairment of cell growth (Nehrbass et al., 1990). Importantly, both *NUP159C* and *NUP159ΔFG* were able to complement the otherwise nonviable *nup159Δ*-null strain under galactose-induced growth conditions (Fig. 3 A). Whereas *NUP159ΔFG* complemented almost like wild-type *NUP159*, *NUP159C* cells grew slower, which, however, is expected because of the lack of the N-terminal β-propeller domain, involved in mRNA export.

Next, we isolated these Nup82 complexes devoid of FG repeats from yeast lysates by tandem affinity purification. The eluates were finally fractionated on a size-exclusion chromatography (SEC) column coupled to MALS. Our method of expression and purification in yeast, which allows obtaining microgram quantities of the heterotetrameric Nup82–Nup159C–Nsp1C–Dyn2 complex resulted in a MALS value in the range of 600–650 kD (Fig. 3 B and Fig. S2, B–D). The heterotetrameric Nup82–Nup159ΔFG–Nsp1C–Dyn2 complex, which includes the N-terminal β-propeller domain of Nup159, was correspondingly

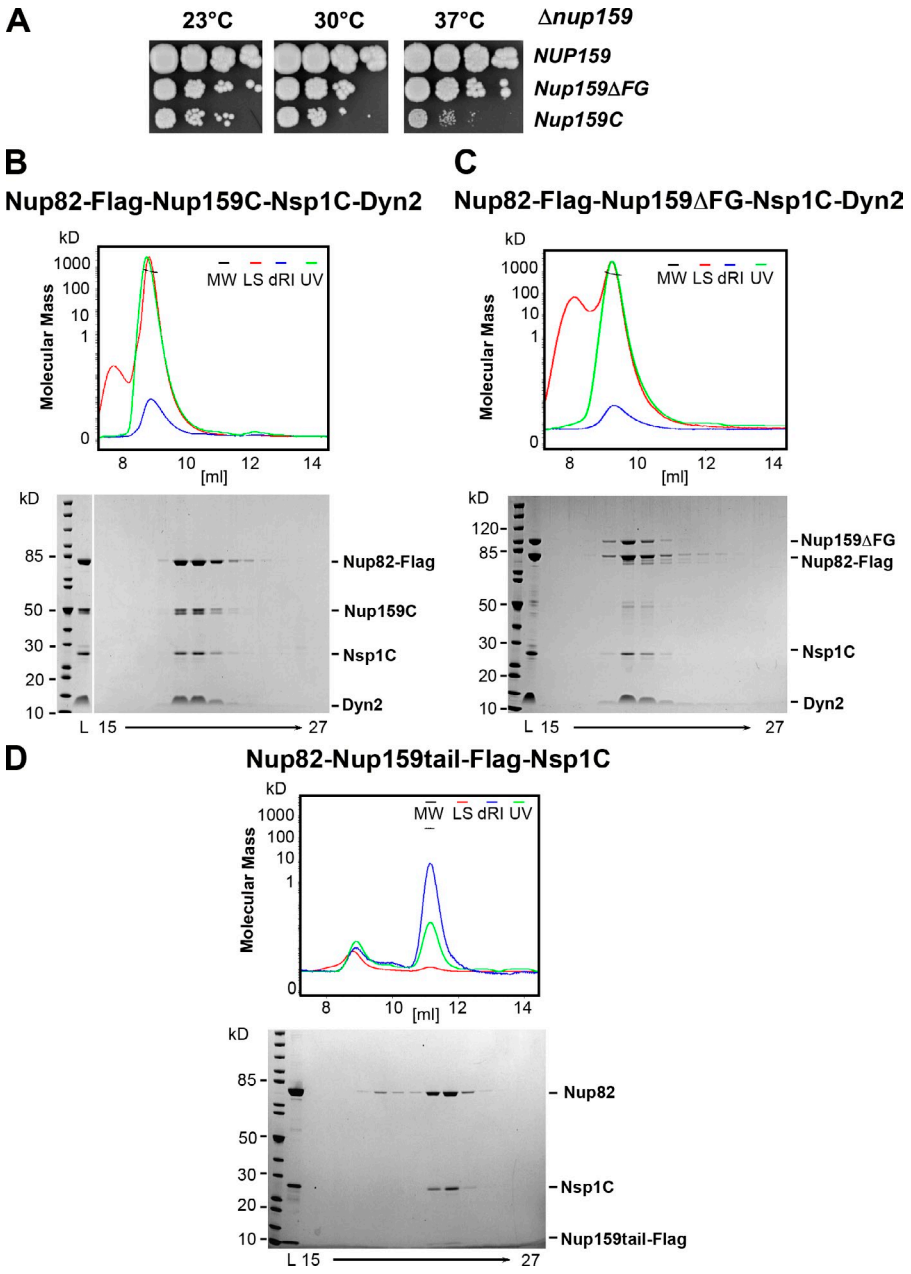


Figure 3. **SEC-MALS analysis of the different in vivo assembled Nup82 complexes.** (A) Growth analysis of yeast *nup159Δ*-null strain complemented with the indicated Nup159 constructs under control of the *GAL1* promoter and used for biochemical and EM analyses. Specifically, the *nup159Δ* shuffle strain was transformed with *LEU2* plasmids carrying wild-type *NUP159*, *nup159ΔFG*, and *nup159C*, respectively. Subsequently, the *URA3-NUP159* shuffle plasmid was shuffled out on galactose-containing 5-FOA plates. Derived yeast colonies complemented by *NUP159*, *nup159ΔFG*, and *nup159C* were spotted onto YPG (yeast extract, peptone, galactose) plates before it was further grown for 5 d. (B) SEC-MALS analysis of the affinity-purified Nup82–Nup159C–Nsp1C–Dyn2 complex, assembled in yeast cells as described in Materials and methods. The differential refractive index (dRI), light scattering (LS), and UV graphs are plotted against the elution volumes from a Superdex 200 Increase 10/300 GL gel filtration column. Two individual Nup82 complex preparations were analyzed by SEC-MALS, yielding a rather high molecular mass (MM) in the range of 650 kD (645 and 672 kD, respectively). The data shown are from a single representative experiment out of two repeats. The white line on the Coomassie-stained gel indicates that the intervening lanes corresponding to fractions 12–14 were removed for presentation purposes. (C) SEC-MALS analysis of the affinity-purified Nup82–Nup159ΔFG–Nsp1C–Dyn2 complex, revealing a molecular mass of 744 kD (calculated molecular mass of Nup159ΔFG, 100 kD). The data shown are from a single representative experiment out of two repeats. (D) SEC-MALS analysis of the affinity-purified Nup82–Nup159tail–Flag-Nsp1C complex, revealing a molecular mass of 114 kD (Nup159 tail fragment has a calculated molecular mass of 8 kD). The data shown are from a single representative experiment out of two repeats. See also Fig. S2 (B–E). L, load.

larger (Fig. 3 C). We were also able to reconstitute a pentameric Nup82 complex that harbored also the Nup116 autocatalytic domain, known to bind to the β propeller of Nup82. All five subunits coeluted at a correspondingly higher molecular weight, although based on Coomassie staining, it appeared that Nup116C might be substoichiometric relative to Nup82 (Fig. S2 E).

To find out how the Nup82 complex isolated from cells under conditions of overexpression compares to the endogenous Nup82 complex, we affinity purified the Nup82 complex (Nup82–Nup159ΔFG*–Nsp1C–Dyn2) from yeast cells, in which all nucleoporin subunits were expressed from their endogenous promoters (Fig. S2, B and C). Although the endogenous Nup82 complex was isolated in ∼10-fold lower amounts when compared with the overproduced complex (Fig. S2 D), we were able to perform SEC-MALS analyses. This revealed that the endogenous Nup82 complex exhibits a similar gel filtration behavior and a related MALS values when compared with the overproduced complex.

We also tested the in vivo assembly of further simplified Nup82 complexes, derived from expression in yeast. In this way, it was possible to assemble and purify a core Nup82–Nsp1C complex devoid of Nup159, but this heterodimer had the tendency to aggregate after purification and was largely found in the void volume during SEC (unpublished data). However, when heterodimeric Nup82–Nsp1C was coexpressed with the short Nup159 tail peptide (Fig. 1 A), a stable heterotrimeric complex could be isolated, which behaved as a monomer of ∼115 kD according to the SEC-MALS measurements (Fig. 3 D). These data suggest a 1:1:1 stoichiometry of the Nup82–Nsp1C–Nup159 tail (theoretical $M_r$ of 123 kD).

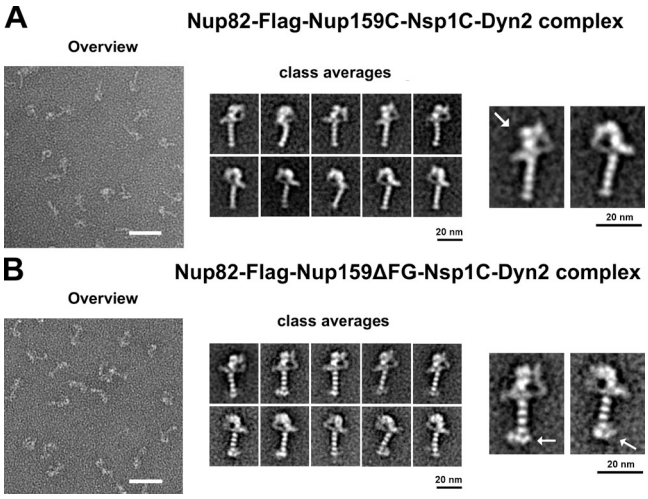


Figure 4. **EM analysis of the purified Nup82 complexes.** (A and B) Electron micrographs of the affinity-purified and GraFix-treated Nup82-Flag–Nup159C–Nsp1C–Dyn2 complex (A) or Nup82-Flag–Nup159ΔFG–Nsp1C–Dyn2 complex (B). Bars, 50 nm. Shown are an overview picture (left), a gallery of the representative class averages determined by multivariate statistical analysis (middle), and two enlarged classes, displaying presumable front and back orientation of the Nup82 complex (right). Arrows indicate distinct globular masses, corresponding to Nup82 β-propeller domains (A) and Nup159 β-propeller domains (B). See also Fig. S3.

## Structure of the Nup82 complex revealed by EM

To gain insight into the morphology of the Nup82–Nup159C–Nsp1C–Dyn2 complex, we sought to analyze its structure using EM. As for the molecular mass determination, we could not observe clear-cut particles of the purified Nup82 complex by negative staining EM when carrying FG repeats (unpublished data). To avoid a possible interference of the natively unfolded FG repeats with the staining procedure on the grid, we analyzed the purified Nup82 complexes devoid of FG repeats by EM, which in this case revealed nicely visible particles in overview micrographs allowing further image processing. By 2D classification of single particles, we were able to visualize for the first time the structure of this NPC module, either as unfixed specimen or fixed by the GraFix (glycerol and glutaraldehyde gradient fixation) method that is based on gentle protein fixation during glycerol–glutaraldehyde gradient centrifugation (Kastner et al., 2008). In both cases, the Nup82 complex exhibits an elongated (~30 nm long) structure, which in several 2D classes resembles an alphabetic letter, P (Fig. 4 A). Because of this feature, we suggest the name "P complex" for the Nup82 module, as opposed to the Y complex for the Nup84 module. Other 2D classes of the Nup82 complex (GraFix), however, reveal in more detail how the 20-nm-long stalk turns into a more globular head structure that forms a ring with a spurlike appendix, resembling the head of a rapier. In line with our premise that 10 copies of Dyn2 interact with two copies of Nup159, we observe the typical stalk structure, which is segmented in five "pearls" that nicely correspond to the $DID_{Nup159}$-Dyn2 rod structure. Each pearl corresponds to a Dyn2 homodimer aligned on a string between two extended $DID_{Nup159}$ strands (Stelter et al., 2007). Accordingly, the apparently asymmetric head structure should be constituted by the α-helically predicted Nup159C and Nsp1C as well as full-length Nup82 composed of a β-propeller N-terminal domain and an α-helical CTD. The head appears to have an intrinsic flexibility and is accordingly less distinct in the unfixed Nup82 complex (Fig. S3 A). We could also determine the EM structure of the Nup82–Nup159ΔFG–Nsp1C–Dyn2 complex, in which Nup159 still contains its N-terminal β-propeller domain (Fig. 3 C). The obtained structure resembles that of the previous complex, but an additional globular mass preceding the DID could be observed corresponding to the Dbp5-recruiting β propeller (Fig. 4 B, arrows). Apparently, the head structure of the Nup82 complex exhibits distinct globular masses, some of which according to their size could correspond to Nup82 β-propeller domains (Fig. 4 A, arrow).

## 3D electron tomography structure of the Nup82 complex

Because the asymmetric structure of the Nup82 complex is quite unexpected for a dimeric assembly, we sought to obtain more insights into its architecture using 3D EM. We acquired 91 tomograms of the negatively stained complex and subsequently processed 5,941 subtomograms according to a previously described procedure (Bui et al., 2013). We first aligned the entire P complex and found that some of its features were averaged out in specific classes (Fig. 5 A). This might be caused by the flexible attachment of the $DID_{Nup159}$-Dyn2 rod to the head that likely limits the overall attainable resolution. We therefore focused the single particle alignment to the head domain that was thus revealed more clearly, while the $DID_{Nup159}$-Dyn2 rod was averaged out (Fig. 5 B and Fig. S4, A and B). The 3D reconstructions indeed revealed a strikingly asymmetric structure with two distinct gaps (Fig. 5 C). The head of the P structure consists of three globular domains and a peripheral spur element and is consistent with the aforementioned 2D analysis. The major asymmetric feature is a rod-shaped connector bridging the spur to the most distant globular domain 3, which is situated only on one side of the complex. In addition, an elongated loop connects the globular domain 3 to the $DID_{Nup159}$-Dyn2 rod, thereby forming the peculiar P structure.

## Hydrodynamic radius and subunit stoichiometry of the Nup82 complex

Our biochemical analysis collectively with the MALS measurements showed that the Nup82 complex self-dimerizes. This is consistent with the overall size of the complex and the number of DID-Dyn2 densities as observed by EM as well as cross-linking data (see following paragraph). However, the accuracy of the light scattering experiments might be limited by the conformational flexibility of the complex as revealed by class averaging, particle interactions on the columns, or contaminants in the peak fraction, which could be large particles (e.g., smearing in from the void) and thus contribute by a strong light scattering. It might thus not be possible to deduce the stoichiometry of the Nup82 complex by simply summing up the molecular weights of possible subunit combinations to match them to the molecular weight obtained by MALS. To address this challenge, we decided to further analyze the SEC-MALS–derived molecular weight of the Nup82 complex by an independent line

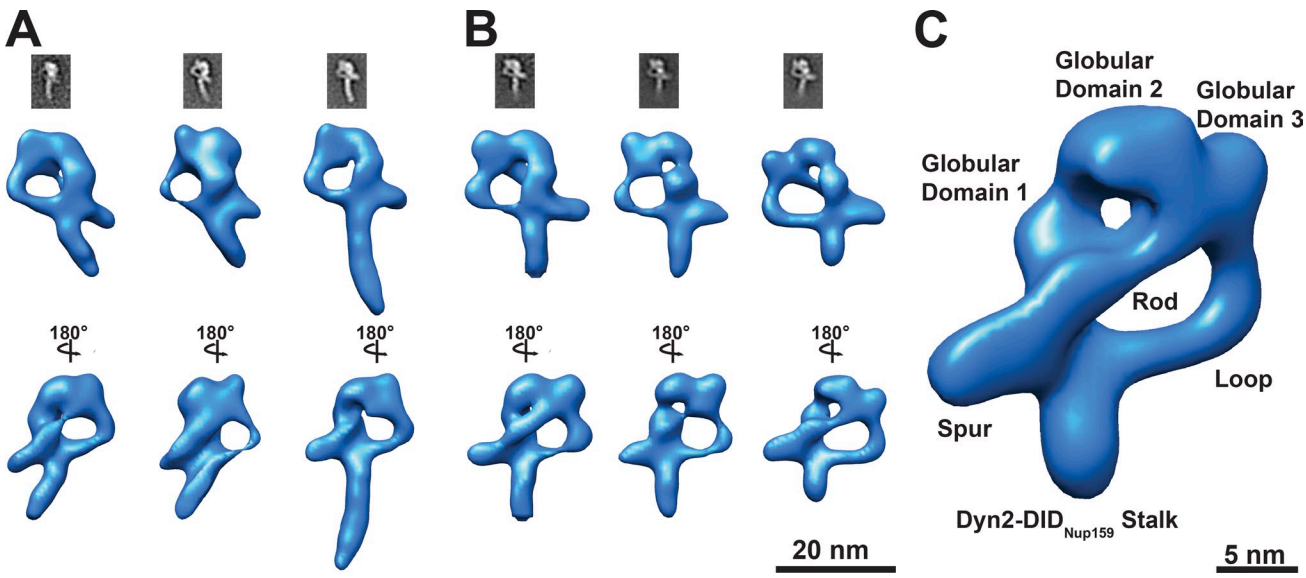


Figure 5. **3D structural analysis of the Nup82–Nup159C–Nsp1C–Dyn2 complex by negative-staining electron tomography.** (A) Representative class averages of affinity-purified Nup82–Nup159C–Nsp1C–Dyn2 complex based on subtomogram averaging. Parts of the $DID_{Nup159}$-Dyn2 stalk are averaged out in the first two classes. (B) Representative class averages of the affinity-purified Nup82–Nup159C–Nsp1C–Dyn2 complex based on subtomogram averaging focused by local masking to the head region such that it is resolved with higher detail. (C) Representative class of the affinity-purified Nup82–Nup159C–Nsp1C–Dyn2 complex. Three globular domains and a spurlike element orthogonal to the stalk build the backbone structure. The globular domains 3 and 1 are connected by a rod element. See also Fig. S4 (A and B).

of evidence. The shape-independent molecular weight of the whole complex can be calculated from the Svedberg equation if the sedimentation coefficient ($s$) and the hydrodynamic radius ($R_h$) are known, as previously described (Trokter et al., 2012). SEC was performed to measure the $R_h$ of the Nup82 complex (Trokter et al., 2012). Moreover, the $R_h$ was also estimated from the shape and EM volume of the Nup82 complex (García de la Torre et al., 2001). Analytical sedimentation velocity ultracentrifugation was performed to evaluate sample homogeneity and to measure the $s$ value $s_{20,w}$ of the complex. Using SEC with protein standard of known hydrodynamic (Stokes) radii, we have calculated the $R_h$ for the Nup82 complex of 8.96 nm, whereas the EM estimation of the $R_h$ value was ~8.4 ± 0.3 nm, depending on the threshold used in computer program Hydromic (see Materials and methods). SEC peak fractions were used for sedimentation velocity runs. Concentration-dependent $s$ values were measured and an $s_{0,20,w}$ value of 10.4 S extrapolated to a protein concentration of 0 µg/ml was determined (Fig. 6). The molecular mass of the Nup82–Nup159C–Nsp1C–Dyn2 complex calculated from the Svedberg equation taking the $R_h$ and $s$ value into account gave a value of 402 kD, supporting the view that the major peak of the SEC is a dimeric complex with the subunits composition of a 2:2:2:10.

To determine the exact stoichiometry of the subunits, we used quantitative MS as previously described (Ori et al., 2013). We used two synthetic, absolutely quantified (AQUA) reference peptides for each protein (Nsp1, Nup82, Nup159, and Dyn2) to measure heavy and light ratios in targeted mode (Fig. 7 B, Fig. S4 D, and Table S5). These two independent measurements per protein yielded highly consistent signals. To control for potential compositional heterogeneity in the purified molecular species, we measured stoichiometries in gel filtration fractions of Nup82–Nup159C–Nsp1C–Dyn2 complex. The subunit stoichiometry of Nup82/Nup159C/Nsp1C/Dyn2 was in overall 1:1:1:5, although slightly elevated levels of Nup82 in the peak fraction (Fig. 7 B) and Nsp1 in the very early eluting fractions were observed (Fig. S4 D). We thus conclude that the majority of all observed molecular species of the P complex contain two copies each of Nup82, Nup159, and Nsp1 and 10 Dyn2 molecules associated with the dimerized DID domain, which corresponds to a theoretical molecular mass of 415 kD. A minority of the molecular species might contain additional copies of Nup82 and Nsp1.

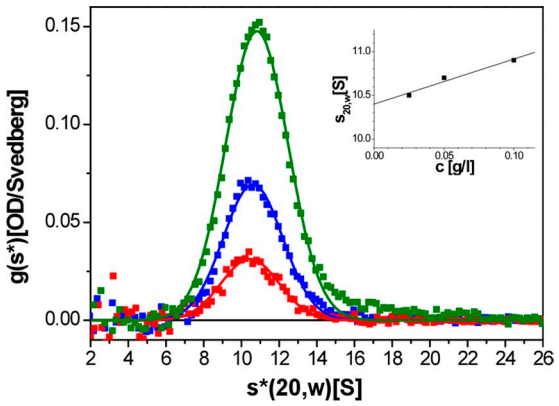


Figure 6. **Sedimentation velocity analysis of the Nup82 complex.** Sedimentation coefficient distribution of the Nup82–Nup159C–Nsp1C–Dyn2 complex measured at three protein concentrations (c), 100 µg/ml (green squares), 50 µg/ml (blue squares), and 25 µg/ml (red squares). Gaussian functions (lines) were fitted to the data. Peak values were extrapolated to a protein concentration of 0 µg/ml (inset), and an $s_{0,20,w}$ value for the main fraction of 10.4 S was observed. The slight increase of the $s$ value with increasing concentration indicates a reversible interaction of the Nup82–Nup159C–Nsp1C–Dyn2 complex. The data shown are from a single representative experiment out of two repeats.

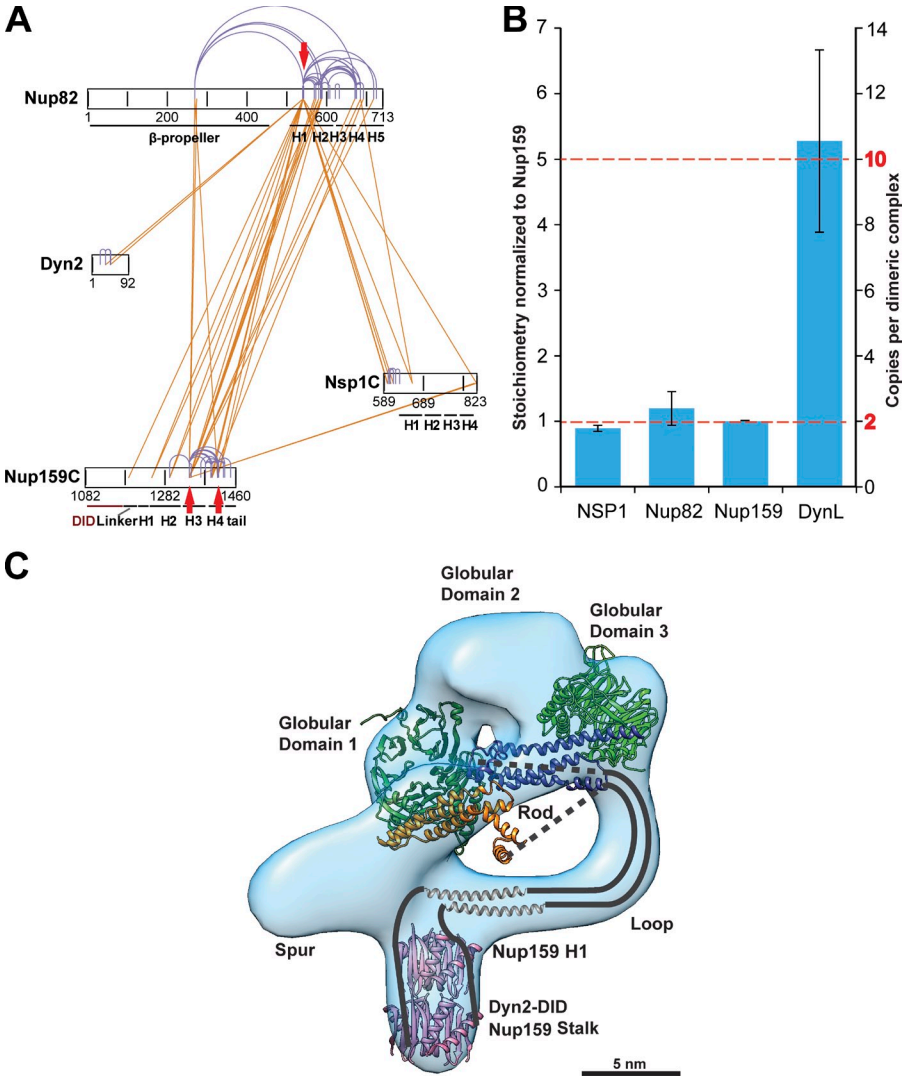


Figure 7. **Quantitative MS, XL-MS, and structural modeling of the Nup82–Nup159C–Nsp1C–Dyn2 complex.** (A) XL-MS of the affinity-purified Nup82–Nup159C–Nsp1C–Dyn2 complex using DSS. The primary structure of the protein is shown, and specific regions are indicated. Interprotein cross-links are shown in orange; intraprotein cross-links are in purple. For the visualization of cross-links, the xiNET tool from the Rappsilber laboratory was used (http://crosslinkviewer.org/index.php). Because multiple copies of each protein are present, the latter might also occur across multiple instances of the same protein. Homodimeric cross-links that connect the two instances of the same lysine residue are indicated with red arrows. (B) Stoichiometry measurements of purified Nup82–Nup159C–Nsp1C–Dyn2 complex by quantitative, targeted proteomics within the apex of the gel filtration peak (Fig. 3 B). Two heavy-labeled reference peptides per protein were used as intrinsic standards. The apparent values were normalized to the abundance of Nup159; error bars correspond to one standard deviation. (C) Structural model illustrating the possible architecture of the Nup82–Nup159C–Nsp1C–Dyn2 complex. Two Nup82–Nup159 heterodimers are shown in green and blue, as well as green and orange, and occupy globular domains 1 and 3, respectively. The N terminus of the Nup159 might proceed through the loop toward Dyn2-$DID_{Nup159}$ stalk (only two of five Dyn2 dimers are shown). The Nup159 H1 domains (gray helices) reside closely to the Dyn2-$DID_{Nup159}$ stalk as shown by the XL-MS analysis. See also Figs. S4 and S5 and Tables S3–S5.

### XL-MS of the Nup82 complex to map interaction surfaces between the subunits

We next analyzed the protein interfaces within the Nup82 complex using cross-linking MS (XL-MS). We cross-linked the tetrameric Nup82-Flag–Nup159C–Nsp1C–Dyn2 complex using two complementary isotope-coded cross-linkers that facilitate the identification of restraints of two different lengths, namely disuccinimidyl-suberate (DSS; ≤35 Å) and disuccinimidyl-glutarate (DSG; ≤30 Å). We identified 90 interprotein and 154 intraprotein links at a false positive discovery rate of 5% using MS according to a previously described procedure (Walzthoeni et al., 2012). The cross-linking experiment confirms the previously shown interfaces between the C-terminal region of Nup159 with the β propeller of Nup82 (Yoshida et al., 2011). However, Nup159 is also strongly engaged with the α-helical, C-terminal part of Nup82 through various contact sites. Fewer restraints are formed with the C and N terminus of Nsp1, which also interacts with α-helical N-terminal part of Nup82. The XL-MS data thus confirm the biochemical analysis described in this paragraph and indicate an interaction hub of all three proteins (Fig. 7 A).

The dimerization property of the P complex precludes the assignment of restraints to a specific single copy of a protein. As a consequence, the identified intraprotein cross-links can in principle account for both contact sites within a protein or across two copies of the same protein. Exceptions are cross-links formed across two instances of the same peptide, which must account for restraints within a homodimer (Fig. 7 A and Fig. S4 C). We identified four of such restraints, which were useful to understand the homodimerization interfaces within the Nup82 complex, namely K1343 and K1414 of Nup159 and K541 and K580 of Nup82. The cross-linking data imply that a homodimeric interface of Nup82 is formed by helical interactions of the C-terminal region (K541 and K580). Nup82 further interacts with the Nup159 C terminus (Yoshida et al., 2011) that also homodimerizes as indicated by homodimeric cross-links of K1343 and K1414 (Fig. 7 A and Fig. S4 C) in addition to the region of Nup159 in which dimerization of the $DID_{Nup159}$-Dyn2 rod and H1 was biochemically observed. We conclude that the P complex dimerizes through multiple contact sites in Nup159 and Nup82.

### Modeling of the central interaction hub of the Nup82 complex

To understand how such a unique structural arrangement might form an overall asymmetric, P-shaped structure, we used an integrated modeling approach (see supplemental material for details). Based on the available high-resolution information of Nup82–159 heterodimer and the Nup159 C-terminal region, we generated a heterodimeric model of Nup82–Nup159 (Fig. S5 A). We next used docking approaches as implemented in HADDOCK that translated the cross-links into distance restraints (Dominguez et al., 2003; de Vries et al., 2007) to model the homodimerization interface. This approach resulted in several clusters of models (Fig. S5 B) of which one is preferred because it is consistent with the EM structure, energetically favored, and satisfies more restraints (Fig. S5 C). The model would suggest that Nup159 forms an asymmetric heterodimeric interface that places the two Nup82 β propellers into the globular domains 1 and 3 (Fig. 7 C). Although ultimate proof by high-resolution structural analysis is required, our structural model offers an explanation for how the dimeric arrangement of the Nup82 complex might possibly be assembled into an asymmetric architecture.

## Discussion

Most of the ∼30 nucleoporins are organized in biochemically stable NPC subcomplexes. Knowledge of their structure is key to locate them in the context of the structural scaffold of the entire NPC (Bui et al., 2013). In this study, we present a structural model of the conserved Nup82 complex. Our data indicate that the essential Nup159C domain forms the structural backbone of the Nup82 complex, along which the other subunits—Nup82, Nsp1, and Dyn2—become organized (Fig. 5 C and Fig. 7 C). Biochemical, biophysical, and EM analyses allow hypothesizing how Nup159C acts as organizer for the whole complex. Key for this scaffolding role is H1 within Nup159C, which cooperates with the upstream linker sequence and DID motif (Fig. 1) to function as a dimerization device that in vivo is essential for NPC assembly. A heptad repeat pattern within H1 exhibits conserved hydrophobic residues at positions 1 and 4, but charged residues at the typical position in between, known to strengthen the coiled-coil dimer, are less prevalent. This could explain the requirement of a second auxiliary dimerization mechanism fulfilled by the $DID_{Nup159}$-Dyn2 array that stabilizes the coiled-coil interaction within H1.

Besides the essential role of H1, the remainder Nup159C subdomains (H2-H4 and tail) are less crucial, at least in vivo as shown by deletion analysis. This finding suggests a certain degree of redundancy in the system, possibly accomplished by the other α-helical regions within Nup82 and Nsp1. We speculate that the α-helical domains of all three subunits, Nup159, Nup82, and Nsp1, form an intricate interaction network, which is consistent with our cross-linking data (Fig. 7 A and Fig. S4 C). Because these α-helical domains are regularly interrupted by helix-breaking residues (Fig. 1 and Fig. S1), they do not form elongated rodlike structures as found in typical coiled-coil proteins (e.g., lamins and spectrins) but may fold into an intertwined array of helical bundles, which could explain the insensitivity toward single helical segment deletions. Consistent with this model, a monomeric Nup82–Nsp1C heterodimer can be efficiently assembled in vivo, which, however, requires the short Nup159 tail fragment for optimal solubility (Fig. 3 D). In addition, the Nup159 tail motif may help to organize the entire Nup82 complex into its asymmetric 3D structure.

Although the stoichiometry of the Nup82 complex intuitively suggests a symmetric organization of the subunits, it strikingly forms an asymmetric structure. Although such an arrangement is not unprecedented, it is very rare. A recent study identified 11 homodimeric structures with pronounced global asymmetry in the protein database (Swapna et al., 2012). Most are nucleic acid-containing protein complexes, in which a specific RNA or DNA sequence provides an asymmetric scaffold onto which the same proteins are assembled in multiple structurally distinct instances. However, also α-helical coiled coils can induce asymmetry (Brown, 2010). In the case of the Nup82 complex, it seems that the C-terminal coiled-coil domains of Nup159 and possibly Nsp1 provide such an asymmetric scaffold. Almost all variants of the P complex investigated in this study, including the endogenously expressed complex, were dimeric, although with stoichiometric variations regarding Dyn2, Nup82, and Nsp1. This biochemically dynamic behavior may imply that the in vivo stoichiometry of the Nup82 complex is dynamic and could vary across cellular conditions with potentially altered RNA export activity.

It is interesting to speculate about the physiological restraints that favored the evolution of an asymmetric Nup82 complex architecture. Those are likely the stoichiometry of the FG nucleoporins and their spatial positioning toward the central channel that were optimized to create a functional permeability barrier and to enable efficient transport. To gain insights into how these FG domains might be positioned toward the central channel, we asked where the Nup82 complex is located within the NPC scaffold. We therefore searched for its structural signature within the human tomographic map of the NPC as previously described (Bui et al., 2013) but were unable to identify highly significant hits. This result might be explained by interspecies differences because it is not yet clear whether the yeast and human nuclear pore have an identical architecture, stoichiometry, or even subcomplex copy numbers. Nevertheless, common to lower and higher eukaryotes is the asymmetric positioning of this subcomplex into the cytoplasmic ring. Such asymmetric density exists in the human NPC and is sufficiently large to accommodate the yeast P-complex structure in two possible orientations (Fig. 8). Because the Nup82 complex in overall is flattened when viewed from the z axis, it can stack well into the ring scaffold of the NPC, i.e., the cytoplasmic ring of dimerized Y-shaped Nup107 complexes, forming basically a rectangle between Y and P complexes (Fig. 8). This arrangement is consistent with the previously reported localization of the human Nup214 complex (Bui et al., 2013) and would indeed allow positioning the FG domains toward the central channel. In this way, the FG repeats could optimally

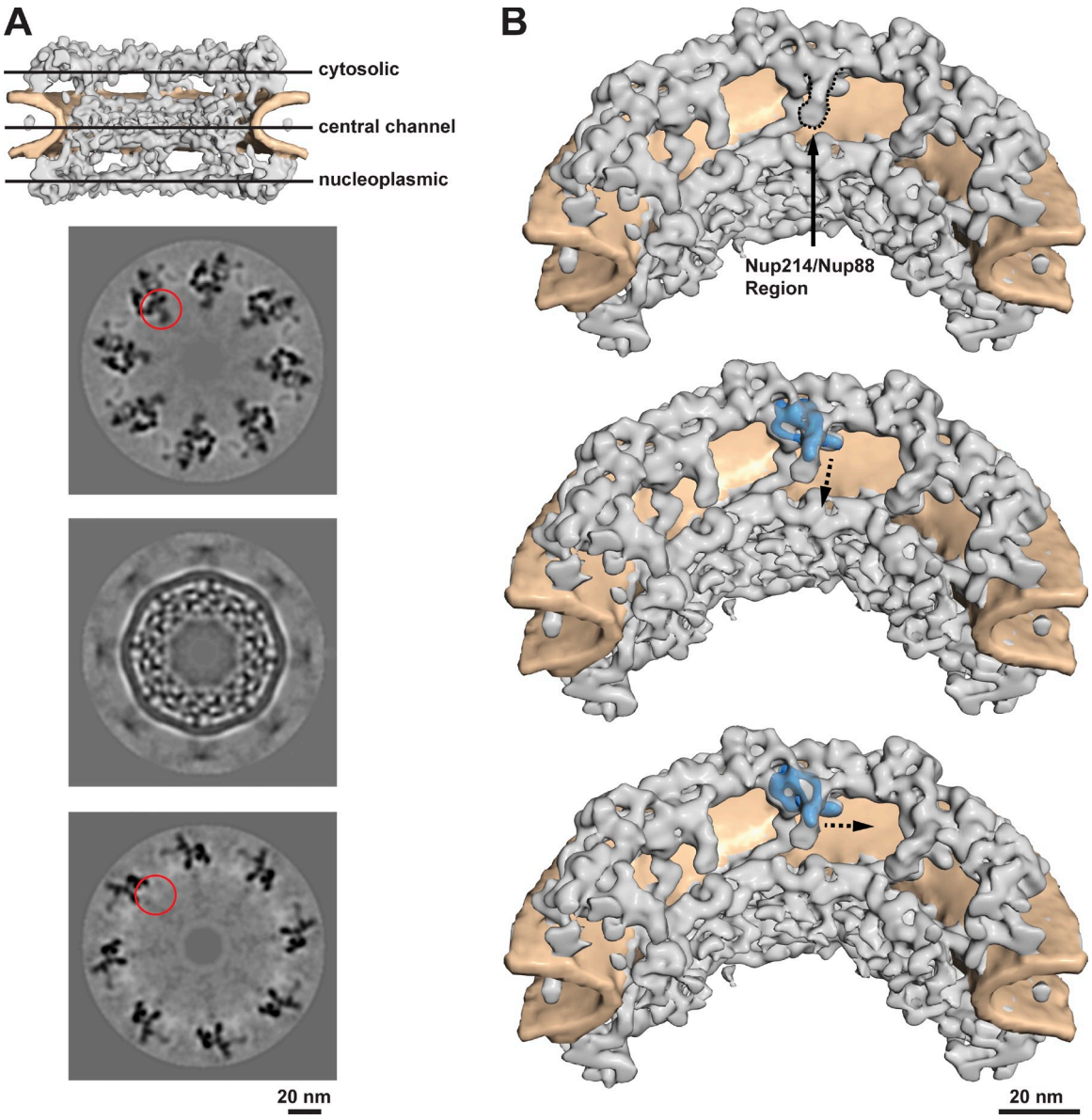


Figure 8. **Potential position of the Nup82–Nup159C–Nsp1C–Dyn2 complex within the human NPC.** (A) Three orthogonal slices through the cytosolic part (top), the central channel (middle), and the nucleoplasmic part (bottom) of the previously published tomographic map of the human NPC are shown. Red circles indicate a region in which additional density is observed in the cytoplasmic ring that could accommodate the P complex. (B) Two possible placements (middle and bottom) of the Nup82–Nup159C–Nsp1C–Dyn2 complex (blue) within the tomographic map of the NPC (top). The progression of the Dyn2-DID$_{Nup159}$ stalk is indicated by dashed arrows.

interact with the shuttling transport receptors but also expose Nup159's N-terminal β-propeller domain, which is crucial for terminating mRNA export at the cytoplasmic face of the NPC.

## Materials and methods

### Plasmids, strains, and yeast growth

Plasmids were generated by standard DNA recombinant procedures and are listed in Table S1. *S. cerevisiae* wild-type and mutant strains harboring the indicated plasmids or chromosomal integrations and used in this study are listed in Table S2. Plasmid transformations into *E. coli* or yeast were performed according to standard protocols. *E. coli* strains were grown in lysogeny broth medium. Exponentially growing yeast cultures were spotted onto YPD (yeast peptone dextrose medium), YPG, and synthetic dextrose complete medium + 5-fluoro-orotic acid (5-FOA) plates in 10-fold serial dilution steps (first spot contained cell suspension of $OD_{600}$ = 1.0). Plates were incubated at the indicated temperatures for 2–5 d. To analyze complementation of yeast-null strains expressing the various wild-type and mutant constructs, shuffle strains were used, carrying the corresponding wild-type copy gene on a *URA3* shuffle plasmid and the mutant allele on either a *TRP1* or *LEU2* plasmid, and were grown on 5-FOA plates.

### Microscope imaging

Cells expressing GFP-tagged proteins were grown to an early log phase at 30°C in YPG or selective media and then shifted to 23°C or 37°C for 2–4 h. Subsequently, cells were pelleted, washed with water, applied onto glass slides (Carl Roth), and examined by fluorescence microscopy without fixation, at room temperature, using a microscope (Imager Z1; Carl Zeiss) equipped with a 100/63×, NA 1.4 Plan Apochromat oil immersion objective lens (Carl Zeiss) and a digital interference contrast third generation or high efficiency EGFP filter set. Pictures were acquired with a camera

(AxioCam MRm; Carl Zeiss) and AxioVision 4.8.2.0 software (Carl Zeiss) at a resolution of 1,388 × 1,040 (binning = 1 × 1, gain factor = 1). Pictures were exported as TIFF files and processed in Photoshop CS 6 (Adobe) for levels. The detailed procedure to localize GFP-tagged proteins using fluorescence microscopy has been described in Bassler et al. (2006).

### Reconstitution of Nup82 complexes in *S. cerevisiae*

To perform simultaneous expression of multiple ORFs of interest in the yeast system, the coding sequences of nucleoporins under investigation were inserted into appropriate yeast expression vectors, as recently described (Thierbach et al., 2013). For Flag-TEV-ProtA affinity purifications, *S. cerevisiae* strain DS1-2b (Nissan et al., 2002) was transformed with corresponding plasmids carrying the respective nucleoporin-encoding genes. Yeast cells were grown at 30°C in synthetic raffinose complete −X−Y medium, and at an $OD_{600}$ of 1.5–2.0, the medium was supplemented with 2% (wt/vol) galactose to induce the *GAL* promoters and grown for additional 4–6 h. The cells were harvested at $OD_{600}$ of 2–3 and lysed in buffer Hepes-NB (20 mM Hepes, pH 7.5, 150 mM NaCl, 50 mM K(OAc), 2.5 mM $Mg(OAc)_2$, 1 mM DTT, 5% glycerol, and 0.01% [vol/vol] NP-40), including FY complete protease inhibitor (Serva) by cryogenic grinding (MM400; Retsch). The lysate was cleared (17,000 rpm for 20 min at 4°C), and the Flag-TEV-ProtA–tagged proteins were affinity purified from the supernatant using IgG-Sepharose beads in suspension (IgG-Sepharose 6 Fast Flow; GE Healthcare). After washing, proteins were eluted by TEV protease in buffer for 90 min at 16°C in a 2.5-ml column (Mobicol; MoBiTec). TEV eluates were incubated with Flag agarose (Sigma-Aldrich) for 1 h at 4°C, washed, and eluted with Flag peptide (Sigma-Aldrich) for 30 min at 4°C. To detect Nup159 in whole cell lysates by Western analysis, monoclonal anti-Nup159 antibody mAB165C10 was used (provided by M. Rout, Rockefeller University, New York, NY).

### Expression and purification of recombinant Nup159 constructs from *E. coli* followed by CD measurements

Recombinant Nup159 $QT_{4–5}$-Linker-H1 and Nup159 $QT_{4–5}$-Linker-h1-5 were expressed in *E. coli* BL21 Codon Plus. Specifically, cells were transformed with pET15b-HIS-Nup159-$QT_{4–5}$-Linker-H1 or pET15b-HIS-Nup159-$QT_{4–5}$-Linker-h1-5 and grown in lysogeny broth medium at 37°C to an $OD_{600}$ of 0.5. Expression was induced with 0.1–0.5 mM IPTG for 3 h at 23°C. Cells were lysed in buffer containing 20 mM Hepes, pH 7.5, 150 mM NaCl, 5% vol/vol glycerol, 1 mM β-mercaptoethanol, and 10 mM imidazole at pH 8.0 supplemented with protease inhibitor (Serva) and by high-pressure cavitation (Microfluidics Corp.) and cleared (17,000 rpm for 15 min at 4°C). 6HIS-tagged proteins were purified from the supernatant with Ni-nitrilotriacetic acid affinity column (QIAGEN) for 2 h at 4°C. After three washing steps with buffer including 10 mM imidazole, 6HIS-tagged proteins were eluted with buffer including a 50–250-mM imidazole gradient.

CD spectra of the protein samples were obtained on a spectropolarimeter (J-720; Jasco) using a water bath and water-jacketed cells for temperature control. Samples for CD measurements were prepared in 10 mM sodium phosphate, pH 7.0, in the protein concentration range of 3–10 µM. Thermal unfolding was measured by monitoring the CD signal at 222 nm in the temperature range of 5–80°C. Reversibility was determined by comparing measurements taken at 5°C before and after thermal unfolding.

### 2D EM and image processing

Negative-staining EM of the truncated Nup82 complex was performed as described previously (Lutzmann et al., 2005). For negative staining, 5 µl of sample was placed on a freshly glow-discharged, carbon-coated grid, allowed to absorb to the carbon for 10 s, washed three times with water, stained with uranyl acetate (2% wt/vol), and dried. Micrographs were recorded using an electron microscope (Tecnai F20; FEI) with a bottom-mounted 4K, high sensitivity charge-coupled device camera (Eagle; FEI) at a nominal magnification of 50,000, operating at 200 kV. 4,000 particles for the Nup82–Nup159C–Nsp1C–Dyn2 complex, 3,416 particles for the unfixed Nup82–Nup159C–Nsp1C–Dyn2 complex, and 5,029 particles for the Nup82–Nup159ΔFG–Nsp1C–Dyn2 complex were selected manually using Boxer (Ludtke et al., 1999). Subsequent image processing was performed in IMAGIC-4D (van Heel et al., 1996), following the program's standard procedures. Particles were band pass filtered and normalized in their gray value distribution and mass centered. Alignment and iterative refinement of class averages followed the procedures described in Lutzmann et al. (2005).

### GraFix of the affinity-purified Nup82 complexes

After purification, Flag-eluted complexes were loaded onto a 200-µl cushion of 7.5% (vol/vol) glycerol in buffer Hepes-NB (20 mM Hepes pH 7.5, 150 mM NaCl, 50 mM K(OAc), 2 mM $Mg(OAc)_2$, and 5% glycerol) followed by a linear 10–30% (vol/vol) glycerol and 0–0.15% glutaraldehyde gradient (Kastner et al., 2008). Samples were centrifuged in a rotor (SW 60 Ti; Beckman Coulter) for 18 h at 50,000 rpm and 4°C before 200-µl fractions were collected and analyzed by a negative-staining EM.

### 3D EM and image processing

Tomograms of the negatively stained Nup82 complex were collected using a transmission electron microscope (Polara; FEI) operated at 100 kV and equipped with a camera of 4,096 × 4,096 pixels (US4000; Gatan) using the SerialEM (Mastronarde, 2005). In total, 91 tomograms were collected over a tilt range of ±60° with anangular increment 3° at binning 2, resulting in a nominal pixel size of 6.06 Å. The defocus was 1.5–3 mm, and the total dose was 300 $e^-/Å^2$. The 3D structure of the Nup82 subcomplex was obtained using a previously described protocol (Bui et al., 2013). Subtomograms of the acquired tomograms from negatively stained Nup82 particles were projected for 2D classification, and the resulting classes were subjected to subtomogram averaging. We manually picked 5,941 particles (subtomograms). Subtomograms were projected along the missing wedge axis to create an equivalent number of 2D images for subsequent 2D classification using k-means clustering in SPIDER (Frank et al., 1996), which resulted in 20 classes. A 3D structure corresponding to each class was then calculated using subtomogram averaging. The resolution of all classes as determined by Fourier shell correlation varied and was 36 Å for the best class. Hydrodynamic radius was estimated using Hydromic (García de la Torre et al., 2001), a computer program used for the prediction of hydrodynamic properties of macromolecular structures determined from EM.

### SEC-MALS

Affinity-purified Nup82 complexes were analyzed by SEC equilibrated in a buffer without NP-40 (20 mM Hepes, pH 7.5, 150 mM NaCl, 50 mM K(OAc), 2.5 mM $Mg(OAc)_2$, and 5% glycerol). They were separated on a Superdex 200 10/300 GL or Superdex 200 Increase 10/300 GL column attached to the ÅKTA Basic system (GE Healthcare).

The chromatography system was connected in series with an eight-angle light scattering detector (DAWN HELEOS; Wyatt Technology Corp.) with a light-scattering refractometer for differential refractive index detection (SEC-3010; WGE Dr Bures) was used to determine the molecular mass of complexes. Data were collected at a flow rate of 0.5 ml/min at 4°C. Measurement analysis were performed using the ASTRA 6.1 software and Zimm light-scattering model (Wyatt Technology Corp.), yielding the molecular mass and mass distribution (polydispersity) of the sample.

### Hydrodynamic radius of the Nup82 complex

The hydrodynamic radius ($R_h$) of the Nup82–Nup159C–Nsp1C–Dyn2 complex was measured by SEC using a Superdex 200 Increase 10/300 GL column (GE Healthcare) equilibrated in a standard buffer (20 mM Hepes, pH 7.5, 150 mM NaCl, 50 mM K(OAc), and 2.5 mM $Mg(OAc)_2$). Proteins standards of known Stokes radii were used for calibration (gel filtration protein standard; Bio-Rad Laboratories): 8.58 nm thyroglobulin, 5.1 nm bovine γ-globulin, 2.8 nm chicken ovalbumin, and 1.9 nm equine myoglobin. Elution volumes were used to plot the calibration curve to calculate the hydrodynamic radius ($R_h$) of the complex as described previously (Trokter et al., 2012).

### Analytical ultracentrifugation

Sedimentation velocity experiments were performed to determine the sedimentation coefficient of the Nup82–Nup159C–Nsp1C–Dyn2 complex. For sedimentation velocity runs, proteins were purified by SEC (Superdex 200 Increase 10/300 GL column) at 6°C in standard buffer (20 mM Hepes, pH 7.5, 150 mM NaCl, 50 mM K(OAc), and 2.5 mM $Mg(OAc)_2$), and peak fractions were immediately loaded in precooled double-sector charcoal-Epon cells in an analytical ultracentrifuge (Optima XL-A; Beckman Coulter). For each sedimentation velocity run, 400 µl of protein sample was analyzed. The protein concentrations were 25–100 µg/ml. Experiments were performed at 6°C, at 42,000 rpm. Scans were recorded at 230 nm using a spacing of 0.003 cm in the continuous scan mode. Data analysis was performed using the program DCDT+ (version 2.4.0; Philo, 2006) that implements the algorithms described by Stafford (1992). The Gaussian function was fitted to sedimentation coefficient distributions to obtain the sedimentation coefficient of the major species. Data were corrected to standard conditions, $s_{20,w}$ (20°C; $H_2O$). The viscosity of the buffer was measured to be 1.52 mPa × second at 6°C using a capillary viscometer (KPG Ubbelohde; Schott).

### Molecular mass determination using the Svedberg equation

The molecular mass of the Nup82 complex was calculated (Trokter et al., 2012) according to the experimentally determined Stokes radii and sedimentation coefficients using the Svedberg equation: $M = 6\pi \times \eta \times N \times R_s \times s/1 - \nu \times \rho$, where M is the molecular mass, $\eta$ is the viscosity of the water at 20°C (0.01 g/cm/s), *N* the Avogadro's number ($6.022 \times 10^{23}$), $R_s$ is the Stokes radius of the protein (nanometer), *s* is the sedimentation coefficient of the complex corrected to standard conditions (at 20°C in water: $s_{20,w}$; $10^{-13}$ *s* [S]), $\nu$ is the partial specific volume of the protein complex at 20°C (0.737 $cm^3/g$; calculated using SEDNTERP V.1.09), and $\rho$ is the density of water at 20°C (1 $g/cm^3$).

### XL-MS

100 µg (0.5 µg/µl) of the affinity-purified Nup82–Nup159C–Nsp1C–Dyn2 complex was cross-linked by the addition of an isostoichiometric mixture of H12/D12 isotope-coded, DSS (Creative Molecules) or DSG (Creative Molecules), respectively. Equal amounts of cross-linker were added eight times every 4 min to a final concentration of 1.6 mM. The cross-linking reactions allowed to proceed for 30 min at 37°C and quenched by addition of ammonium bicarbonate to a final concentration of 50 mM for 10 min at 37°C. Cross-linked proteins were denatured using urea and RapiGest (Waters) at a final concentration of 4 M and 0.05% (wt/vol), respectively. Samples were reduced using 10 mM DTT (30 min at 37°C), and cysteines were carbamidomethylated with 15 mM iodoacetamide (30 min in the dark). Protein digestion was performed first using 1:100 (wt/wt) LysC (Wako Pure Chemical Industries) for 4 h at 37°C and then finalized with 1:50 (wt/wt) trypsin (Promega) overnight at 37°C, after the urea concentration was diluted to 1.5 M. Samples were then acidified with 10% (vol/vol) trifluoroacetic acid and desalted using MicroSpin columns (Harvard Apparatus) following the manufacturer's instructions. Cross-linked peptides were enriched using SEC as described by Leitner et al. (2012). In brief, desalted peptides were reconstituted with SEC buffer (30% [vol/vol] acetonitrile [ACN] in 0.1% [vol/vol] trifluoroacetic acid) and fractionated using a Superdex Peptide PC 3.2/30 column (GE Healthcare) on a liquid chromatography system (Ettan; GE Healthcare) at a flow rate of 50 µl/min. Fractions eluting between 0.9 and 1.4 ml were evaporated to dryness and reconstituted in 20–50 µl of 5% (vol/vol) ACN in 0.1% (vol/vol) formic acid (FA) according to 215-nm absorbance. Between 2% and 10% of the amount contained in the collected SEC fractions were analyzed by liquid chromatography–coupled tandem MS (MS/MS) using an ultraperformance liquid chromatography (UPLC) system (nanoAcquity; Waters) connected online to a mass spectrometer instrument (LTQ-Orbitrap Velos Pro; Thermo Fisher Scientific). Peptides were separated on a BEH300 C18 (75 mm × 250 mm; 1.7 mm) nanoAcquity UPLC column using a stepwise 60- or 120-min gradient between 3% and 85% (vol/vol) ACN in 0.1% (vol/vol) FA. Data acquisition was performed using a TOP-20 strategy in which survey-MS scans (mass/charge range of 375–1,600) were acquired in the Orbitrap (R = 30,000), and ≤20 of the most abundant ions per full scan were fragmented by collision-induced dissociation (normalized collision energy = 40; activation Q = 0.250) and analyzed in the LTQ. To focus the acquisition on larger cross-linked peptides, charge states 1, 2, and unknown were rejected. Dynamic exclusion was enabled with repeat count = 1, exclusion duration = 60 s, list size = 500, and mass window ± 15 ppm. Ion target values were 1,000,000 (or 500 ms maximum fill time) for full scans and 10,000 (or 50 ms maximum fill time) for MS/MS scans. All the samples were analyzed in technical duplicates. To assign the fragment ion spectra, raw files were converted to centroid mzXML using the Mass Matrix file converter tool and then searched using xQuest (Walzthoeni et al., 2012) against a FASTA database containing the sequences of the cross-linked proteins. Posterior probabilities were calculated using xProphet (Walzthoeni et al., 2012), and results were filtered using the following parameters: false discovery rate = 0.05, minimum δ score = 0.95, MS1 tolerance window of 4–7 ppm, and linear discriminant score > 25.

### SRM-MS

Selected reaction monitoring assays were developed as described in Ori et al. (2014) using a spectral library derived from the affinity-purified Nup82–Nup159C–Nsp1C–Dyn2 complex. The purified complex was applied to SEC (Fig. 3 B), and the fractionated proteins were denatured using urea and RapiGest at a final concentration of 4 M and 0.05% (wt/vol), respectively, and digested as described in the previous paragraph. The digested peptides were analyzed by shotgun MS on an Orbitrap Velos Pro as described in the previous section apart from the following parameters: Data acquisition was performed using a TOP-10 strategy in which survey-MS scans (mass/charge range of 375–1,600) were acquired in the Orbitrap (R = 30,000), and ≤10 of the most abundant ions per full scan were fragmented by higher energy collision-induced dissociation (normalized collision energy = 40; activation Q = 0.1) and analyzed in the Orbitrap (R = 7,500). Ion target values were 1,000,000 (or 500 ms maximum fill time) for full scans and 30,000 (or 150 ms maximum fill time) for MS/MS scans.

Raw files were searched against a database containing the four complex members using Mascot (v. 2.2.07; Matrix Science). A spectral library was built using Skyline (v. 2.5.0.5675; MacLean et al., 2010), and for each protein, two proteotypic peptides were selected as described in Ori et al. (2014). For each peptide, ≤10 transitions were derived from the spectral library by selecting the most intense y-series ions. Isotopically labeled and AQUA versions of the selected peptides were purchased (AQUA Ultimate; Thermo Fisher Scientific). Synthetic peptides were pooled and analyzed on a mass spectrometer (TSQ Vantage; Thermo Fisher Scientific) to refine the SRM assays by selecting the five most intense transitions per peptide. To determine the stoichiometry of the Nup82–Nup159C–Nsp1C–Dyn2 complex, AQUA peptides were spiked into the SEC fractions in equimolar amount before protein digestion. SRM assays for both the endogenous (light) and reference (heavy) peptides were recorded in schedule mode using a TSQ Vantage triple quadrupole mass spectrometer connected to a nanoAcquity UPLC system. Digested peptides were separated on a BEH300 C18 (75 µm × 250 mm; 1.7 µm) nanoAcquity UPLC column with a 75-min linear gradient between 3 and 35% (vol/vol) ACN and 0.1% (vol/vol) FA at a flow rate of 300 nl/min. Data were recorded with an unscheduled data acquisition scheme using a fixed dwell time of 20 ms per transition. Peptide concentrations were estimated relatively to the reference AQUA peptides using the summed intensity of all transitions. Peptides corresponding to the same protein were averaged and normalized to the Nup159 signal, resulting in the final stoichiometric readout. SRM assay refinement, recalibrations, and data analysis were performed using SpectroDive (Biognosys AG).

### Structural modeling

Searches for structures of acceptable homology to the C-terminal, α-helical part of Nup159 were not successful. In particular, searches for structural homologues with BLAST (Basic Local Alignment Search Tool; Altschul et al., 1990), PSI-BLAST (Position-Specific Iterated BLAST; Altschul et al., 1997), and the HMMER webserver (Finn et al., 2011) did not yield any significant templates. Models for the C-terminal, α-helical part of Nup159 were thus generated using the I-TASSER webserver (Roy et al., 2010). Five top-ranking clusters were generated. The two best clusters (according to their c scores; Zhang, 2008) shared a common fold for the C-terminal, α-helical part of Nup159 (including parts of H2, H3, H4, and the tail region; aa 1,286–1,434), resembling an α-helical bundle. Therefore, after structural alignment ($C_\alpha$ root-mean-square deviation < 3.5 Å), this model was used to build a heterodimer with the C-terminal Nup82 β propeller. To generate a structural model of the Nup159–Nup82 heterodimer, the model of the C-terminal, α-helical part of Nup159 and the x-ray structure of the C-terminal Nup82 β-propeller (PDB ID: 3PBP; Yoshida et al., 2011) were superimposed with their overlapping counterpart of the Nup82–Nup159–Nup98 heterotrimeric x-ray structure (PDB ID: 3TKN; Stuwe et al., 2012). In the crystal structure, only 28 out of 39 residues of the construct are visible in the crystal structure, pointing to disordered termini. The tail region of the model for the Nup159 helices and the 28 residues present in the crystal are essentially identical ($C_\alpha$ root-mean-square deviation < 0.6 Å), and, after superposition of the Nup159 helices, only few minor side chain–side chain clashes with Nup82 were observed through visual inspection. The heterodimeric model Nup159–Nup82 was further refined to optimize its interface energetics. The HADDOCK webserver refinement protocol was used (de Vries et al., 2010; Kastritis and Bonvin, 2010). This ensured that all potentially missing side chains were properly built, and the interface of the complex was optimized using the optimized potentials for liquid simulations force field (Jorgensen and Tirado-Rives, 1988), and nonbonded interactions were calculated using a cutoff of 8.5 Å. Electrostatic energy ($E_{elec}$) was calculated by a shift function, whereas a switching function (between 6.5 and 8.5 Å) was used for the van der Waals energy ($E_{vdw}$). Desolvation energy is calculated by implementing empirical atomic solvation parameters (Fernández-Recio et al., 2004). This procedure generated 20 Nup159–Nup82 models, starting from different random velocities. As is default in the HADDOCK protocol, the average score of the top 4 models was evaluated, and the top model was selected for further docking experiments. All calculations were performed with HADDOCK version 2.1/Crystallography and Nuclear Magnetic Resonance System version 1.2 (Brunger, 2007) through the refinement interface of the HADDOCK web server. To construct the tetrameric complex composed of two Nup159–Nup82

heterodimers, the guru interface of HADDOCK was used for docking calculations (de Vries et al., 2010). XL-MS data were implemented as interaction restraints. They were set to have an effective (and maximum) $C_\alpha$ – $C_\alpha$ distance of 35.2 Å, whereas the minimum distance was only defined by energetics. This distance was selected as a result of the analogy of the maximum $C_\alpha$ distance that the DSS cross-linker may have, when cross-linking Lys side chains. For docking calculations, the standard HADDOCK protocol was used (Dominguez et al., 2003) with minor modifications: 10,000 structures were generated in the first iteration (*it0*; randomization and energy minimization step) instead of the default 1,000 to increase sampling. Standard HADDOCK scoring for *it0* was applied to select the 400 top-ranking structures that are subsequently passed onto the next docking step (semiflexible simulated annealing [SA]). The semiflexible SA (*it1*) is composed by several steps, including a high-temperature rigid body search, rigid body SA, semiflexible SA with flexible side chains at the interface, and then semiflexible SA with fully flexible interface (both backbone and side chains). Final refinement in explicit water is similar to the one described in the previous paragraph, but the number of generated models was increased to 400 to improve sampling. Using the aforementioned protocol, two docking runs were performed, one concerning only homodimeric cross-links of Nup159 (K1343, K1414) and another incorporating three additional cross-links of Nup159 with Nup82 (Nup82 K269 with Nup159 K1343; Nup82 K269 with Nup159 K1414; and Nup82 K274 with Nup159 K1343). Because it is not clear whether the three aforementioned cross-links fall into one of the two Nup82–Nup159 heterodimers or occur between the two heterodimers, these cross-links were treated with an either–or logical statement during the modeling. The two docking runs yielded clusters that were subsequently evaluated using the buried surface area criterion. The buried surface area was calculated with Crystallography and Nuclear Magnetic Resonance System (Brunger, 2007) and has been shown to correlate to the binding free energy of rigid binders in a near-quantitative manner (Kastritis and Bonvin, 2013a,b). In short, from docking run (a) various clusters were generated with much smaller buried surface area compared with docking run (b), in which a single well-defined cluster was eventually generated. The best structure of the cluster was subsequently used for fitting to the EM 3D averages using University of California, San Francisco Chimera (Pettersen et al., 2004).

### Multiple sequence alignment

Protein sequences were aligned using T-Coffee and Jalview (Waterhouse et al., 2009). Secondary structures were predicted using Jpred (Cole et al., 2008).

### Online supplemental material

Fig. S1 shows multisequence alignment of CTD of Nup159. Fig. S2 shows expression levels of Nup159 mutant constructs in yeast and comparison of overproduced and endogenous Nup82–Nup159ΔFG–Nsp1C–Dyn2 complexes. Fig. S3 shows negative-staining EM analysis and SEC of the unfixed and GraFix-treated Nup82–Nup159C–Nsp1C–Dyn2 complex. Fig. S4 shows the EM structure, cross-linking, and stoichiometry of the purified Nup82 complex. Fig. S5 shows structural modeling of the interaction between Nup82 and Nup159. Tables S1 and S2 show plasmids and strains used in this study, respectively. Table S3 shows interprotein cross-links identified within the Nup82 complex using DSS. Table S4 shows interprotein cross-links identified within the Nup82 complex using DSG. Table S5 shows the peptides used as heavy reference in the SRM-MS experiments. Online supplemental material is available at http://www.jcb.org/cgi/content/full/jcb.201411003/DC1.

We thank Beate Jannack for excellent technical assistance and the EM core facility at Heidelberg University headed by Dr. Stefan Hillmer, with Dr. Ingrid Hausser and Dr. Jacomine Krijnse Locker as scientific staff for providing technical support for transmission EM. We also thank Mike Rout for the monoclonal anti-Nup159 antibody mAB165C10.

E. Hurt and D. Flemming are recipients of grants from the Deutsche Forschungsgemeinschaft (SFB 638/B2). K.H. Bui was supported by postdoctoral fellowships from the Swiss National Science Foundation, the European Molecular Biology Organization, and Marie Curie Actions. M. Beck acknowledges funding by the European Research Council (309271-NPCAtlas). This work was supported by National Institutes of Health grant GM 084276 to E. Barbar.

The authors declare no competing financial interests.

Submitted: 3 November 2014
Accepted: 22 December 2014

## References

Altschul, S.F., W. Gish, W. Miller, E.W. Myers, and D.J. Lipman. 1990. Basic local alignment search tool. *J. Mol. Biol.* 215:403–410. http://dx.doi.org/10.1016/S0022-2836(05)80360-2

Altschul, S.F., T.L. Madden, A.A. Schäffer, J. Zhang, Z. Zhang, W. Miller, and D.J. Lipman. 1997. Gapped BLAST and PSI-BLAST: a new generation of protein database search programs. *Nucleic Acids Res.* 25:3389–3402. http://dx.doi.org/10.1093/nar/25.17.3389

Bailer, S.M., C. Balduf, J. Katahira, A. Podtelejnikov, C. Rollenhagen, M. Mann, N. Pante, and E. Hurt. 2000. Nup116p associates with the Nup82p-Nsp1p-Nup159p nucleoporin complex. *J. Biol. Chem.* 275:23540–23548. http://dx.doi.org/10.1074/jbc.M001963200

Bailer, S.M., C. Balduf, and E. Hurt. 2001. The Nsp1p carboxy-terminal domain is organized into functionally distinct coiled-coil regions required for assembly of nucleoporin subcomplexes and nucleocytoplasmic transport. *Mol. Cell. Biol.* 21:7944–7955. http://dx.doi.org/10.1128/MCB.21.23.7944-7955.2001

Barbar, E. 2008. Dynein light chain LC8 is a dimerization hub essential in diverse protein networks. *Biochemistry*. 47:503–508. http://dx.doi.org/10.1021/bi701995m

Bassler, J., M. Kallas, and E. Hurt. 2006. The NUG1 GTPase reveals and N-terminal RNA-binding domain that is essential for association with 60 S pre-ribosomal particles. *J. Biol. Chem.* 281:24737–24744. http://dx.doi.org/10.1074/jbc.M604261200

Beck, M., F. Förster, M. Ecke, J.M. Plitzko, F. Melchior, G. Gerisch, W. Baumeister, and O. Medalia. 2004. Nuclear pore complex structure and dynamics revealed by cryoelectron tomography. *Science*. 306:1387–1390. http://dx.doi.org/10.1126/science.1104808

Belgareh, N., C. Snay-Hodge, F. Pasteau, S. Dagher, C.N. Cole, and V. Doye. 1998. Functional characterization of a Nup159p-containing nuclear pore subcomplex. *Mol. Biol. Cell*. 9:3475–3492. http://dx.doi.org/10.1091/mbc.9.12.3475

Bernad, R., H. van der Velde, M. Fornerod, and H. Pickersgill. 2004. Nup358/RanBP2 attaches to the nuclear pore complex via association with Nup88 and Nup214/CAN and plays a supporting role in CRM1-mediated nuclear protein export. *Mol. Cell. Biol.* 24:2373–2384. http://dx.doi.org/10.1128/MCB.24.6.2373-2384.2004

Brown, J.H. 2010. How sequence directs bending in tropomyosin and other two-stranded α-helical coiled coils. *Protein Sci.* 19:1366–1375. http://dx.doi.org/10.1002/pro.415

Brunger, A.T. 2007. Version 1.2 of the Crystallography and NMR system. *Nat. Protoc.* 2:2728–2733. http://dx.doi.org/10.1038/nprot.2007.406

Bui, K.H., A. von Appen, A.L. DiGuilio, A. Ori, L. Sparks, M.T. Mackmull, T. Bock, W. Hagen, A. Andrés-Pons, J.S. Glavy, and M. Beck. 2013. Integrated structural analysis of the human nuclear pore complex scaffold. *Cell*. 155:1233–1243. http://dx.doi.org/10.1016/j.cell.2013.10.055

Cole, C., J.D. Barber, and G.J. Barton. 2008. The Jpred 3 secondary structure prediction server. *Nucleic Acids Res.* 36(Suppl. 2):W197–W201.

Del Priore, V., C. Heath, C. Snay, A. MacMillan, L. Gorsch, S. Dagher, and C. Cole. 1997. A structure/function analysis of Rat7p/Nup159p, an essential nucleoporin of *Saccharomyces cerevisiae*. *J. Cell Sci.* 110:2987–2999.

Delphin, C., T. Guan, F. Melchior, and L. Gerace. 1997. RanGTP targets p97 to RanBP2, a filamentous protein localized at the cytoplasmic periphery of the nuclear pore complex. *Mol. Biol. Cell*. 8:2379–2390. http://dx.doi.org/10.1091/mbc.8.12.2379

de Vries, S.J., A.D. van Dijk, M. Krzeminski, M. van Dijk, A. Thureau, V. Hsu, T. Wassenaar, and A.M. Bonvin. 2007. HADDOCK versus HADDOCK: new features and performance of HADDOCK2.0 on the CAPRI targets. *Proteins*. 69:726–733. http://dx.doi.org/10.1002/prot.21723

de Vries, S.J., M. van Dijk, and A.M. Bonvin. 2010. The HADDOCK web server for data-driven biomolecular docking. *Nat. Protoc.* 5:883–897. http://dx.doi.org/10.1038/nprot.2010.32

Dominguez, C., R. Boelens, and A.M. Bonvin. 2003. HADDOCK: a protein-protein docking approach based on biochemical or biophysical information. *J. Am. Chem. Soc.* 125:1731–1737. http://dx.doi.org/10.1021/ja026939x

Doye, V., and E. Hurt. 1997. From nucleoporins to nuclear pore complexes. *Curr. Opin. Cell Biol.* 9:401–411. http://dx.doi.org/10.1016/S0955-0674(97)80014-2

Fahrenkrog, B., and U. Aebi. 2003. The nuclear pore complex: nucleocytoplasmic transport and beyond. *Nat. Rev. Mol. Cell Biol.* 4:757–766. http://dx.doi.org/10.1038/nrm1230

Fernández-Recio, J., M. Totrov, and R. Abagyan. 2004. Identification of protein-protein interaction sites from docking energy landscapes. *J. Mol. Biol.* 335:843–865. http://dx.doi.org/10.1016/j.jmb.2003.10.069

Finn, R.D., J. Clements, and S.R. Eddy. 2011. HMMER web server: interactive sequence similarity searching. *Nucleic Acids Res.* 39(Suppl. 2):W29–W37. http://dx.doi.org/10.1093/nar/gkr367

Fornerod, M., J. van Deursen, S. van Baal, A. Reynolds, D. Davis, K.G. Murti, J. Fransen, and G. Grosveld. 1997. The human homologue of yeast CRM1 is in a dynamic subcomplex with CAN/Nup214 and a novel nuclear pore component Nup88. *EMBO J.* 16:807–816. http://dx.doi.org/10.1093/emboj/16.4.807

Frank, J., M. Radermacher, P. Penczek, J. Zhu, Y. Li, M. Ladjadj, and A. Leith. 1996. SPIDER and WEB: processing and visualization of images in 3D electron microscopy and related fields. *J. Struct. Biol.* 116:190–199. http://dx.doi.org/10.1006/jsbi.1996.0030

Frey, S., R.P. Richter, and D. Görlich. 2006. FG-rich repeats of nuclear pore proteins form a three-dimensional meshwork with hydrogel-like properties. *Science*. 314:815–817. http://dx.doi.org/10.1126/science.1132516

García de la Torre, J., O. Llorca, J.L. Carrascosa, and J.M. Valpuesta. 2001. HYDROMIC: prediction of hydrodynamic properties of rigid macromolecular structures obtained from electron microscopy images. *Eur. Biophys. J.* 30:457–462. http://dx.doi.org/10.1007/s002490100176

Gorsch, L.C., T.C. Dockendorff, and C.N. Cole. 1995. A conditional allele of the novel repeat-containing yeast nucleoporin RAT7/NUP159 causes both rapid cessation of mRNA export and reversible clustering of nuclear pore complexes. *J. Cell Biol.* 129:939–955. http://dx.doi.org/10.1083/jcb.129.4.939

Grandi, P., S. Emig, C. Weise, F. Hucho, T. Pohl, and E.C. Hurt. 1995a. A novel nuclear pore protein Nup82p which specifically binds to a fraction of Nsp1p. *J. Cell Biol.* 130:1263–1273. http://dx.doi.org/10.1083/jcb.130.6.1263

Grandi, P., N. Schlaich, H. Tekotte, and E.C. Hurt. 1995b. Functional interaction of Nic96p with a core nucleoporin complex consisting of Nsp1p, Nup49p and a novel protein Nup57p. *EMBO J.* 14:76–87.

Harbury, P.B., T. Zhang, P.S. Kim, and T. Alber. 1993. A switch between two-, three-, and four-stranded coiled coils in GCN4 leucine zipper mutants. *Science*. 262:1401–1407. http://dx.doi.org/10.1126/science.8248779

Hodge, C.A., H.V. Colot, P. Stafford, and C.N. Cole. 1999. Rat8p/Dbp5p is a shuttling transport factor that interacts with Rat7p/Nup159p and Gle1p and suppresses the mRNA export defect of xpo1-1 cells. *EMBO J.* 18:5778–5788. http://dx.doi.org/10.1093/emboj/18.20.5778

Hurt, E.C. 1988. A novel nucleoskeletal-like protein located at the nuclear periphery is required for the life cycle of *Saccharomyces cerevisiae*. *EMBO J.* 7:4323–4334.

Hurwitz, M.E., and G. Blobel. 1995. NUP82 is an essential yeast nucleoporin required for poly(A)$^+$ RNA export. *J. Cell Biol.* 130:1275–1281. http://dx.doi.org/10.1083/jcb.130.6.1275

Jorgensen, W.L., and J. Tirado-Rives. 1988. The OPLS [optimized potentials for liquid simulations] potential functions for proteins, energy minimizations for crystals of cyclic peptides and crambin. *J. Am. Chem. Soc.* 110:1657–1666. http://dx.doi.org/10.1021/ja00214a001

Kastner, B., N. Fischer, M.M. Golas, B. Sander, P. Dube, D. Boehringer, K. Hartmuth, J. Deckert, F. Hauer, E. Wolf, et al. 2008. GraFix: sample preparation for single-particle electron cryomicroscopy. *Nat. Methods*. 5:53–55. http://dx.doi.org/10.1038/nmeth1139

Kastritis, P.L., and A.M. Bonvin. 2010. Are scoring functions in protein-protein docking ready to predict interactomes? Clues from a novel binding affinity benchmark. *J. Proteome Res.* 9:2216–2225. http://dx.doi.org/10.1021/pr9009854

Kastritis, P.L., and A.M. Bonvin. 2013a. Molecular origins of binding affinity: seeking the Archimedean point. *Curr. Opin. Struct. Biol.* 23:868–877. http://dx.doi.org/10.1016/j.sbi.2013.07.001

Kastritis, P.L., and A.M. Bonvin. 2013b. On the binding affinity of macromolecular interactions: daring to ask why proteins interact. *J. R. Soc. Interface*. 10:20120835. http://dx.doi.org/10.1098/rsif.2012.0835

Köhler, A., and E. Hurt. 2010. Gene regulation by nucleoporins and links to cancer. *Mol. Cell*. 38:6–15. http://dx.doi.org/10.1016/j.molcel.2010.01.040

Kraemer, D., R.W. Wozniak, G. Blobel, and A. Radu. 1994. The human CAN protein, a putative oncogene product associated with myeloid leukemogenesis, is a nuclear pore complex protein that faces the cytoplasm. *Proc. Natl. Acad. Sci. USA*. 91:1519–1523. http://dx.doi.org/10.1073/pnas.91.4.1519

Kraemer, D.M., C. Strambio-de-Castillia, G. Blobel, and M.P. Rout. 1995. The essential yeast nucleoporin NUP159 is located on the cytoplasmic side of the nuclear pore complex and serves in karyopherin-mediated binding of transport substrate. *J. Biol. Chem.* 270:19017–19021. http://dx.doi.org/10.1074/jbc.270.32.19017

Leitner, A., R. Reischl, T. Walzthoeni, F. Herzog, S. Bohn, F. Förster, and R. Aebersold. 2012. Expanding the chemical cross-linking toolbox by the use of multiple proteases and enrichment by size exclusion chromatography. *Mol. Cell. Proteomics*. 11:M111.014126. http://dx.doi.org/10.1074/mcp.M111.014126

Lim, R.Y.H., B. Fahrenkrog, J. Köser, K. Schwarz-Herion, J. Deng, and U. Aebi. 2007. Nanomechanical basis of selective gating by the nuclear pore complex. *Science*. 318:640–643. http://dx.doi.org/10.1126/science.1145980

Ludtke, S.J., P.R. Baldwin, and W. Chiu. 1999. EMAN: semiautomated software for high-resolution single-particle reconstructions. *J. Struct. Biol.* 128:82–97. http://dx.doi.org/10.1006/jsbi.1999.4174

Lutzmann, M., R. Kunze, K. Stangl, P. Stelter, K.F. Tóth, B. Böttcher, and E. Hurt. 2005. Reconstitution of Nup157 and Nup145N into the Nup84 complex. *J. Biol. Chem.* 280:18442–18451. http://dx.doi.org/10.1074/jbc.M412787200

MacLean, B., D.M. Tomazela, N. Shulman, M. Chambers, G.L. Finney, B. Frewen, R. Kern, D.L. Tabb, D.C. Liebler, and M.J. MacCoss. 2010. Skyline: an open source document editor for creating and analyzing targeted proteomics experiments. *Bioinformatics*. 26:966–968. http://dx.doi.org/10.1093/bioinformatics/btq054

Makio, T., D.L. Lapetina, and R.W. Wozniak. 2013. Inheritance of yeast nuclear pore complexes requires the Nsp1p subcomplex. *J. Cell Biol.* 203:187–196. http://dx.doi.org/10.1083/jcb.201304047

Martínez, N., A. Alonso, M.D. Moragues, J. Pontón, and J. Schneider. 1999. The nuclear pore complex protein Nup88 is overexpressed in tumor cells. *Cancer Res.* 59:5408–5411.

Mastronarde, D.N. 2005. Automated electron microscope tomography using robust prediction of specimen movements. *J. Struct. Biol.* 152:36–51. http://dx.doi.org/10.1016/j.jsb.2005.07.007

Montpetit, B., N.D. Thomsen, K.J. Helmke, M.A. Seeliger, J.M. Berger, and K. Weis. 2011. A conserved mechanism of DEAD-box ATPase activation by nucleoporins and InsP6 in mRNA export. *Nature*. 472:238–242. http://dx.doi.org/10.1038/nature09862

Napetschnig, J., G. Blobel, and A. Hoelz. 2007. Crystal structure of the N-terminal domain of the human protooncogene Nup214/CAN. *Proc. Natl. Acad. Sci. USA*. 104:1783–1788. http://dx.doi.org/10.1073/pnas.0610828104

Nehrbass, U., H. Kern, A. Mutvei, H. Horstmann, B. Marshallsay, and E.C. Hurt. 1990. NSP1: a yeast nuclear envelope protein localized at the nuclear pores exerts its essential function by its carboxy-terminal domain. *Cell*. 61:979–989. http://dx.doi.org/10.1016/0092-8674(90)90063-K

Nissan, T.A., J. Bassler, E. Petfalski, D. Tollervey, and E. Hurt. 2002. 60S preribosome formation viewed from assembly in the nucleolus until export to the cytoplasm. *EMBO J.* 21:5539–5547. http://dx.doi.org/10.1093/emboj/cdf547

Noble, K.N., E.J. Tran, A.R. Alcázar-Román, C.A. Hodge, C.N. Cole, and S.R. Wente. 2011. The Dbp5 cycle at the nuclear pore complex during mRNA export II: nucleotide cycling and mRNP remodeling by Dbp5 are controlled by Nup159 and Gle1. *Genes Dev.* 25:1065–1077. http://dx.doi.org/10.1101/gad.2040611

Nyarko, A., and E. Barbar. 2011. Light chain-dependent self-association of dynein intermediate chain. *J. Biol. Chem.* 286:1556–1566. http://dx.doi.org/10.1074/jbc.M110.171686

Ori, A., N. Banterle, M. Iskar, A. Andrés-Pons, C. Escher, H. Khanh Bui, L. Sparks, V. Solis-Mezarino, O. Rinner, P. Bork, et al. 2013. Cell type-specific nuclear pores: a case in point for context-dependent stoichiometry of molecular machines. *Mol. Syst. Biol.* 9:648. http://dx.doi.org/10.1038/msb.2013.4

Ori, A., A. Andrés-Pons, and M. Beck. 2014. The use of targeted proteomics to determine the stoichiometry of large macromolecular assemblies. *Methods Cell Biol.* 122:117–146. http://dx.doi.org/10.1016/B978-0-12-417160-2.00006-0

Pettersen, E.F., T.D. Goddard, C.C. Huang, G.S. Couch, D.M. Greenblatt, E.C. Meng, and T.E. Ferrin. 2004. UCSF Chimera—a visualization system for exploratory research and analysis. *J. Comput. Chem.* 25:1605–1612. http://dx.doi.org/10.1002/jcc.20084

Philo, J.S. 2006. Improved methods for fitting sedimentation coefficient distributions derived by time-derivative techniques. *Anal. Biochem.* 354:238–246. http://dx.doi.org/10.1016/j.ab.2006.04.053

Rout, M.P., J.D. Aitchison, A. Suprapto, K. Hjertaas, Y. Zhao, and B.T. Chait. 2000. The yeast nuclear pore complex: composition, architecture, and transport mechanism. *J. Cell Biol.* 148:635–651. http://dx.doi.org/10.1083/jcb.148.4.635

Roy, A., A. Kucukural, and Y. Zhang. 2010. I-TASSER: a unified platform for automated protein structure and function prediction. *Nat. Protoc.* 5:725–738. http://dx.doi.org/10.1038/nprot.2010.5

Schmitt, C., C. von Kobbe, A. Bachi, N. Panté, J.P. Rodrigues, C. Boscheron, G. Rigaut, M. Wilm, B. Séraphin, M. Carmo-Fonseca, and E. Izaurralde. 1999. Dbp5, a DEAD-box protein required for mRNA export, is recruited to the cytoplasmic fibrils of nuclear pore complex via a conserved interaction with CAN/Nup159p. *EMBO J.* 18:4332–4347. http://dx.doi.org/10.1093/emboj/18.15.4332

Stafford, W.F., III. 1992. Boundary analysis in sedimentation transport experiments: a procedure for obtaining sedimentation coefficient distributions using the time derivative of the concentration profile. *Anal. Biochem.* 203:295–301. http://dx.doi.org/10.1016/0003-2697(92)90316-Y

Stelter, P., R. Kunze, D. Flemming, D. Höpfner, M. Diepholz, P. Philippsen, B. Böttcher, and E. Hurt. 2007. Molecular basis for the functional interaction of dynein light chain with the nuclear-pore complex. *Nat. Cell Biol.* 9:788–796. http://dx.doi.org/10.1038/ncb1604

Stelter, P., R. Kunze, M. Radwan, E. Thomson, K. Thierbach, M. Thoms, and E. Hurt. 2012. Monitoring spatiotemporal biogenesis of macromolecular assemblies by pulse-chase epitope labeling. *Mol. Cell*. 47:788–796. http://dx.doi.org/10.1016/j.molcel.2012.06.015

Stuwe, T., L.S. von Borzyskowski, A.M. Davenport, and A. Hoelz. 2012. Molecular basis for the anchoring of proto-oncoprotein Nup98 to the cytoplasmic face of the nuclear pore complex. *J. Mol. Biol.* 419:330–346. http://dx.doi.org/10.1016/j.jmb.2012.03.024

Swapna, L.S., K. Srikeerthana, and N. Srinivasan. 2012. Extent of structural asymmetry in homodimeric proteins: prevalence and relevance. *PLoS ONE*. 7:e36688. http://dx.doi.org/10.1371/journal.pone.0036688

Thierbach, K., A. von Appen, M. Thoms, M. Beck, D. Flemming, and E. Hurt. 2013. Protein interfaces of the conserved Nup84 complex from *Chaetomium thermophilum s*hown by crosslinking mass spectrometry and electron microscopy. *Structure*. 21:1672–1682. http://dx.doi.org/10.1016/j.str.2013.07.004

Thompson, K.S., C.R. Vinson, and E. Freire. 1993. Thermodynamic characterization of the structural stability of the coiled-coil region of the bZIP transcription factor GCN4. *Biochemistry*. 32:5491–5496. http://dx.doi.org/10.1021/bi00072a001

Tran, E.J., Y. Zhou, A.H. Corbett, and S.R. Wente. 2007. The DEAD-box protein Dbp5 controls mRNA export by triggering specific RNA:protein remodeling events. *Mol. Cell*. 28:850–859. http://dx.doi.org/10.1016/j.molcel.2007.09.019

Trokter, M., N. Mücke, and T. Surrey. 2012. Reconstitution of the human cytoplasmic dynein complex. *Proc. Natl. Acad. Sci. USA*. 109:20895–20900. http://dx.doi.org/10.1073/pnas.1210573110

van Deursen, J., J. Boer, L. Kasper, and G. Grosveld. 1996. G2 arrest and impaired nucleocytoplasmic transport in mouse embryos lacking the proto-oncogene CAN/Nup214. *EMBO J.* 15:5574–5583.

van Heel, M., G. Harauz, E.V. Orlova, R. Schmidt, and M. Schatz. 1996. A new generation of the IMAGIC image processing system. *J. Struct. Biol.* 116:17–24. http://dx.doi.org/10.1006/jsbi.1996.0004

von Lindern, M., S. van Baal, J. Wiegant, A. Raap, A. Hagemeijer, and G. Grosveld. 1992. Can, a putative oncogene associated with myeloid leukemogenesis, may be activated by fusion of its 3′ half to different genes: characterization of the set gene. *Mol. Cell. Biol.* 12:3346–3355.

Walzthoeni, T., M. Claassen, A. Leitner, F. Herzog, S. Bohn, F. Förster, M. Beck, and R. Aebersold. 2012. False discovery rate estimation for cross-linked peptides identified by mass spectrometry. *Nat. Methods*. 9:901–903. http://dx.doi.org/10.1038/nmeth.2103

Waterhouse, A.M., J.B. Procter, D.M. Martin, M. Clamp, and G.J. Barton. 2009. Jalview Version 2—a multiple sequence alignment editor and analysis workbench. *Bioinformatics*. 25:1189–1191. http://dx.doi.org/10.1093/bioinformatics/btp033

Weirich, C.S., J.P. Erzberger, J.M. Berger, and K. Weis. 2004. The N-terminal domain of Nup159 forms a β-propeller that functions in mRNA export by tethering the helicase Dbp5 to the nuclear pore. *Mol. Cell*. 16:749–760. http://dx.doi.org/10.1016/j.molcel.2004.10.032

Yoshida, K., H.-S. Seo, E.W. Debler, G. Blobel, and A. Hoelz. 2011. Structural and functional analysis of an essential nucleoporin heterotrimer on the cytoplasmic face of the nuclear pore complex. *Proc. Natl. Acad. Sci. USA*. 108:16571–16576. http://dx.doi.org/10.1073/pnas.1112846108

Zhang, Y. 2008. I-TASSER server for protein 3D structure prediction. *BMC Bioinformatics*. 9:40. http://dx.doi.org/10.1186/1471-2105-9-40